Direct numerical simulation of a pulverized coal jet flame employing a global volatile matter reaction scheme based on detailed reaction mechanism

Takumi Hara[a], Masaya Muto[a], Tomoaki Kitano[a], Ryoichi Kurose[*,a], Satoru Komori[a]

[a]*Department of Mechanical Engineering and Science, and Advanced Research Institute of Fluid Science and Engineering, Kyoto University, Kyoto daigaku-Katsura, Nishikyo-ku, Kyoto 615–8540, Japan*

Abstract

A two-step global reaction scheme for the volatile matter of coal is proposed, and the unsteady coal particle and combustion behaviors in a turbulent pulverized coal jet flame are investigated by performing a direct numerical simulation (DNS) employing the proposed global reaction scheme. The two-step global reaction scheme is constructed to take into account the properties of the volatile matter such as transport coefficients, laminar flame speed and unburned gas temperature and to be applicable to various coal types, and it is validated by comparing the results with those obtained by the detailed reaction mechanism which includes 158 chemical species and 1804 reactions. The validity of the DNS is also assessed by comparing the results with those in the previous experiment (Hwang *et al*., Energy & Fuels, 2005), and the unsteady coal particle motions and combustion characteristics are examined in detail. The results show that the proposed two-step global reaction scheme for the volatile matter of coal can precisely predict the laminar flame speed and burned gas temperature for various coal types from bituminous to low-rank coals over wide ranges of conditions of equivalence ratios, pressures and unburned gas temperatures. In addition, it can correctly take into account the effects of dilutions by H_2O and CO_2 which compromise the evaporated moisture from coal and products of char reaction. It is also verified that a lab-scale turbulent pulverized coal jet flame is well predicted by the DNS em-

[*]Corresponding author.
Email address: `kurose@mech.kyoto-u.ac.jp` (Ryoichi Kurose)

ploying the proposed global reaction scheme. That is, the pulverized coal particles' velocity and its fluctuation and the characteristics of particle preferential motions are in general agreement with those observed in the experiment. The DNS reveals that in the turbulent pulverized coal jet flame, there appear premix and diffusion flame layers inside and outside, respectively. In addition, the reaction of the volatile matter and O_2 in coal-carrier air occurs in the inner premixed flame layer, whereas the reactions of the volatile matter and CO and O_2 in surrounding air occur in the outer diffusion flame layer.

Key words: Pulverized coal combustion; Direct numerical simulation; Volatile matter; Two-step global reaction scheme; Jet flame

1. Introduction

Coal occupies the position of a major primary energy source internationally because of its low procurement costs attributed to the large amount of recoverable reserves, widespread reserves, and stable supply. However, since coal-fired power generation produces large amounts of pollutants, such as SO_x (sulfur oxide) and NO_x (nitrogen oxide), it is important to improve efficiency and to reduce the burden on the environment if we wish to continue using coal as a major source of energy in the future.

Most coal-fired power plants employ pulverized coal combustion in which finely ground coal with particles several tens of micrometers in size is transported into the furnace with air and burned. The combustion process that occurs within the pulverized coal boiler is extremely complex as it involves several elementary processes such as the dispersion of particles in the flow field, heat transfer between the particles and their surrounding air, release of flammable gases (volatile matter) from the particles, heterogeneous reactions, and gas-phase reactions, all of which are greatly affected by turbulence. Therefore, obtaining detailed information that cannot be measured (e.g., flow field, temperature field, concentration field, and the behavior of the pulverized coal particles) using numerical simulations is considered invaluable in designing and developing furnaces efficiently. As a calculation method for such information, a RANS (Reynolds-Averaged Navier-Stokes) simulation (e.g., [1–7]) to solve flow fields

and scalar fields in an averaged time period and a LES (Large-Eddy Simulation) (e.g., [8–14]) to solve flow fields and scalar fields by taking only relatively large-scale turbulence fluctuations into account are being researched. A DNS (Direct Numerical Simulation), which does not use either a turbulence model or a turbulent-chemistry interaction model, can reproduce the effects of the turbulence on the abovementioned elementary processes with greater accuracy than that achieved by the RANS simulation and LES, and DNS is expected to become a useful method for understanding the phenomenon of pulverized coal combustion in turbulence. However, researches employing DNS involve enormous calculation costs. Therefore, few studies have been conducted on virtual or simple pulverized coal flames (e.g., Luo *et al.* [15]), meaning that calculations employing the data of actual pulverized coal flames and detailed comparative reviews with the experimental data have not been conducted in any study. In fact, Luo *et al.* [15] performed a DNS of a pulverized coal flame referring to the experiment [16] targeted here. However, the calculation conditions such as initial gaseous temperature and Reynolds number, and coal characteristics in Luo *et al.* [15] are quite different from those in the experiment [16].

In order to conduct such numerical simulations on pulverized coal combustion, a physical models are needed for the handling of the pulverized coal particles, and improving the accuracy of the model is a major challenge. In particular, the gas-phase reaction of volatile matter of coal is an extremely important elementary process that controls the behavior of pulverized coal combustion. However, the modelling of the reaction has not been discussed sufficiently. The reason for this lies in the facts that the volatile matter is a gas mixture consisting of light gases such as CH_4, CO, CO_2, and water vapor (H_2O) and tars, including aromatic compounds, and that the composition of these gases significantly differs depending on the type of coal [17]. This makes it difficult to apply a uniform reaction model. Previous researches often disregarded the effects of such complex compositions on the gas-phase reaction and instead used a model where the volatile matter was replaced with CH_4 (e.g., [7, 8, 15]). This is one of the reasons why the accuracy of predictions by the numerical simulations of pulverized coal combustion is compromised. For example, Stein *et al.* [11] conducted an LES for

3

pulverized coal combustion and suggested that the reaction model used for the volatile matter was the cause behind the discrepancy between the predicted O_2 concentrations and measured values.

The purpose of this study is, therefore, to propose a precise global reaction scheme for the volatile matter of coal, and to investigate the coal particle and combustion behaviors in a turbulent pulverized coal jet flame by performing the DNS employing the proposed global reaction scheme. The global reaction scheme is constructed to take into account the properties of the complicated volatile matter such as transport coefficients, laminar flame speed and unburned gas temperature and to be applicable to various coal types. The validity of the DNS is assessed by comparing the results with those of the previous experiment [16], and the unsteady coal particle motions and combustion characteristics are examined in detail.

2. Global Reaction Scheme for Volatile Matter of Coal

2.1. Construction Procedure

Owing to the different molecular structures of the volatile matter of coals, their compositions differ with the coal types. Further, the volatile matter yield and its compositions strongly depend on the coal heating temperature and heating rate, because the release of the volatile matter is related to chemical reactions. Therefore, it is very difficult to identify the volatile matter yield and its compositions for each coal through experiments. In this study, the global reaction scheme for the volatile matter of coal is constructed in the following manner.

2.1.1. Determination of Compositions based on Ultimate Analysis and Proximate Analysis

The devolatilization rate and compositions of the volatile matter of coal can be obtained using coal pyrolysis models such as CPD (Chemical Percolation Devolatilization) model [18], FG-DVC model [19] and FLASHCHAIN model [20]. In this study, the NLG (Nitrogen and Light Gas species) version of CPD model [18] is used to predict the amounts of light gases such as CH_4, H_2O, CO_2, CO, H_2, C_2H_6, C_2H_4, C_3H_8 and

4

C_3H_6, and tar in the volatile matter. The compositions of H_2, C_2H_6, C_2H_4, C_3H_8 and C_3H_6 in the light gases and the tar are given under the following assumptions:

i) A 0.4% mass fraction of H_2 in coal is generated.

ii) Light gases C_2H_6, C_2H_4, C_3H_8 and C_3H_6 are generated in mass fraction ratios of 1 : 1 : 0.5 : 1 in addition to CH_4, H_2O, CO_2, CO and H_2.

iii) Tar is composed of C_6H_6 (benzene).

The first and second assumptions are based on the results of the pulverized coal pyrolysis experiment by Xu and Tomita [17]. The third assumption is employed because the calculation of the laminar flame speed based on the detailed reaction mechanism is limited to monocyclic aromatic hydrocarbons at present. It should be noted that the amount of H_2 strongly affects the combustion characteristics, and that the density of the volatile matter changes with the composition of tar. Therefore, these approximations need to be improved in future for more advanced calculations.

In order to take into account the effect of heating rate on the composition of the volatile matter, the numerical simulations of the pyrolysis of coal using the CPD model [18] are carried out for three coal heating rates: 1.0×10^4 K/s, 1.0×10^5 K/s and 1.0×10^6 K/s. The initial coal temperature and the pyrolysis maximum temperature are set to be 300 and 1300 K, respectively. The pyrolysis is found to finish at less than 1300 K in the CPD model, so that the pyrolysis maximum temperature is set to be 1300 K, here. In all, 16 types of coals are used; this includes 14 types of coals used by Xu and Tomita [17] and Newlands coal and Adaro coal. Their properties are listed in Table 1, and the relation of coal atomic H/C ratio and O/C ratio (van Krevelen diagram [21]) is also shown in Fig. 1. Here, Wandoan coal, Hunter Valley coal, Liddell coal, Newvale coal, Yubari Shinko coal, and Newlands coal are classified into bituminous coal, and the other coals are classified into low-rank coals such as sub-bituminous and brown coals. The input parameters for the CPD model [18] were obtained from the proximate and ultimate analysis through the correlation of Genetti *et al.* [22]

Figure 2 shows the effects of carbon content and heating rate on volatile matter yield for the 16 coals. Here, the carbon content is based on a dry-ash-free (daf) basis. Figure 3 also shows the effects of carbon content and heating rate on mass fraction of

chemical species in volatile matter for the 16 coals. It is found that with increasing the carbon contents, the volatile matter yield decreases, the hydrocarbon compositions increase and H_2O, CO_2 and CO decrease, and that the increase in the heating rate tends to slightly increase the tar mass fraction and decrease the mass fractions of the other components. Figure 4 shows the relation of volatile matter atomic H/C (b/a) ratio and O/C (c/a) ratio for the 16 coals. Here, a, b and c correspond to those in the postulated substance, $C_aH_bO_c$, which represents the volatile matter. This suggests a rough correlation between H/C and O/C.

2.1.2. Examination of Combustion Characteristics for a One-dimensional Premixed Flame by Considering a Detailed Reaction Mechanism

Laminar flame speed, s_L, is one of the most important properties of a combustible mixture, i.e., fuel. It depends on equivalence ratio, ϕ, pressure , P, unburned gas temperature, T_u, and so on. It is also essential to use the exact burned gas temperature, T_b, especially for precisely predicting NO_x, whose dependency on T_b is very high. In the pulverized coal combustion, moreover, the values of s_L and T_b are affected not only by coal properties, but also by the moisture evaporating from coal and products because of the char reaction, that is H_2O and CO_2. Therefore, a volatile matter reaction model is essential for adequately accounting for the effects of ϕ, P, T_u and concentrations of dilution gases of H_2O and CO_2 on s_L and T_b.

By considering the light gases and tar as fuel, which are identified in the previous section, and air as oxidizer, numerical simulations of one-dimensional premixed flames are carried out in various ϕ, P and T_u conditions. Then, the obtained values of s_L and T_b are referred to in constructing a two-step global reaction scheme. For the numerical simulation, FlameMaster [23] and a detailed reaction mechanism with 158 chemical species and 1804 reactions as proposed by Narayanaswamy *et al.* [24] are used. Newlands coal, Adaro coal and Yallourn coal are considered, and the conditions are varied in the ranges of P of 0.1–1.0 MPa, T_u of 300–700 K and ϕ of 0.6–1.8. In addition, the dilution rate of the volatile matter by H_2O and CO_2, DR, is varied. Here, DR is the mass ratio of the diluted gas to the volatile matter.

6

2.1.3. Construction of Global Reaction Scheme

Properties. It is desirable to employ the detailed reaction mechanism of the volatile matter of coal in performing the numerical simulations of pulverized coal combustion. However, it is not realistic at present owing to its high computational costs. Therefore, it is assumed that the volatile matter is represented by a postulated substance, $C_aH_bO_c$, as described before. The estimate methods for the molecular weight of $C_aH_bO_c$, $W_{C_aH_bO_c}$, specific heat at constant pressure, C_p, enthalpy, H, entropy, S, thermal conductivity, λ, viscosity, μ, and diffusion coefficient, D, are explained as follows.

The thermodynamic properties, i.e., C_p, H, S are given by NASA polynomials as a function of temperature, T, [25] as

$$\frac{C_p(T)}{R} = a_1 + a_2T + a_3T^2 + a_4T^3 + a_5T^4, \tag{1}$$

$$\frac{H(T)}{RT} = a_1 + \frac{a_2}{2}T + \frac{a_3}{3}T^2 + \frac{a_4}{4}T^3 + \frac{a_5}{5}T^4 + \frac{a_6}{T}, \tag{2}$$

$$\frac{S(T)}{R} = a_1 \ln T + a_2T + \frac{a_3}{2}T^2 + \frac{a_4}{3}T^3 + \frac{a_5}{4}T^4 + a_7. \tag{3}$$

(e.g., CHEMKIN [26]). Here, a_i ($i = 1, 2, ..., 7$) are the coefficients of the polynomials. Also, λ and μ are obtained according to CHEMKIN [27] as

$$\ln \lambda = d_1 + d_2 \ln T + d_3 \left(\ln T\right)^2 + d_4 \left(\ln T\right)^3, \tag{4}$$

$$\ln \mu = e_1 + e_2 \ln T + e_3 \left(\ln T\right)^2 + e_4 \left(\ln T\right)^3. \tag{5}$$

Here, d_i and e_i ($i = 1, 2, ..., 4$) are the coefficients of the polynomials. The diffusion coefficient of chemical species k, D_k, is set under the assumption of the unity Lewis number ($Le = 1$, $D_k = \lambda/\rho C_p$). The values of $W_{C_aH_bO_c}$ and the coefficients, a_i, d_i and e_i, are modeled for the volatile matter by introducing functions, $f_X(b/a, c/a)$. Here, X is replaced by W for $W_{C_aH_bO_c}$, a for a_i, d for d_i, and e for e_i, respectively, and f_X is given as functions of b/a and c/a (see Fig. 4). Accordingly, $W_{C_aH_bO_c}$ is given as

$$W_{C_aH_bO_c} = W_{C_aH_bO_c,\text{ref}} f_W \left(b/a, c/a\right). \tag{6}$$

Here, $W_{C_a H_b O_c, \mathrm{ref}} = 35.0$ g/mol. The coefficients, a_i, for C_p, H, and S in Eqs. $(1) - (3)$ are given as

$$a_i = a_{i, \mathrm{ref}} f_{ai} \left(b/a, c/a \right). \tag{7}$$

Here, $a_{i, \mathrm{ref}}$ are the reference coefficients of the polynomials. Table 2 lists the values of $a_{i, \mathrm{ref}}$, where $a_{i, \mathrm{ref}}$ for $T \in [300; 1000]$ K and $T \in [1000; 3000]$ K are referred to as $a_{i, \mathrm{refL}}$ and $a_{i, \mathrm{refH}}$, respectively. The values of a_6 and a_7 for $T \in [1000; 3000]$ K are given in order to smoothly connect at $T = 1000$ K as

$$[H(1000)]_{\mathrm{L}} = [H(1000)]_{\mathrm{H}}, \tag{8}$$

$$[S(1000)]_{\mathrm{L}} = [S(1000)]_{\mathrm{H}}. \tag{9}$$

Here, subscriptions L and H represent the values using $a_{i, \mathrm{refL}}$ and $a_{i, \mathrm{refH}}$, respectively. The coefficients, d_i, for λ in Eq. (4) are given as

$$d_i = \begin{cases} d_{i, \mathrm{ref}} + \ln f_d \left(b/a, c/a \right) & (i = 1), \\ d_{i, \mathrm{ref}} & (i = 2, 3, 4). \end{cases} \tag{10}$$

Here, $d_{i, \mathrm{ref}}$ are the reference coefficients of the polynomials. The form of this equation is the same as that of the equation of e_i for μ in Eq. (5). Table 3 lists the values of $d_{i, \mathrm{ref}}$ and $e_{i, \mathrm{ref}}$. Above functions, $f_X (b/a, c/a)$ (i.e., f_W, f_{a_i}, f_d and f_e), are assumed to be given by following polynomials.

$$f_X \left(\frac{b}{a}, \frac{c}{a} \right) = \xi_{X,1} + \xi_{X,2} \left(\frac{b}{a} \right) + \xi_{X,3} \left(\frac{c}{a} \right) + \xi_{X,4} \left(\frac{b}{a} \right)^2 + \xi_{X,5} \left(\frac{c}{a} \right)^2 + \xi_{X,6} \left(\frac{b}{a} \right) \left(\frac{c}{a} \right). \tag{11}$$

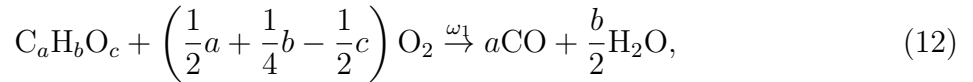Here, the values of the coefficients, $\xi_{X,i}$, are listed in Table 4.

Figure 5 shows the effects of volatile matter compositions (b/a and c/a) on $W_{C_a H_b O_c}$, μ, and λ for the 16 coals at $T = 1000$ K. Here, the curved surface and red plots indicate

the values obtained by the proposed model and CHEMKIN [26, 27], respectively. The red plots generally terminate on the curved surface, implying that the models proposed here are adequate to predict the values of $W_{C_aH_bO_c}$, μ, and λ for various coals under conditions of various heating rates.

Reaction Scheme. The values of the laminar flame speed, s_L, and burned gas temperature, T_b, obtained using the detailed reaction mechanism described in the previous section are the targets in modeling the global reaction scheme. Franzelli *et al.* [28, 29] proposed two-step global reaction schemes for kerosene and CH_4, which are able to precisely predict the values of s_L and T_b, and are at present widely used for both premixed and diffusion combustions [30–33]. According to Franzelli *et al.* [28, 29], the two-step global reaction scheme is modified for the volatile matter of coal in this study, as described following Eqs. (12) – (19). Since the heating rate does not have large influence on the components of the volatile matter especially in the conditions of high heating rates, as shown in Figs. 2 and 3, the heating rate of 1.0×10^6 K/s is adopted here.

The reaction of the volatile matter is assumed to be the following a two-step global reaction:

$$C_aH_bO_c + \left(\frac{1}{2}a + \frac{1}{4}b - \frac{1}{2}c\right)O_2 \xrightarrow{\omega_1} aCO + \frac{b}{2}H_2O, \tag{12}$$

$$CO + \frac{1}{2}O_2 \underset{\omega_{2r}}{\overset{\omega_{2f}}{\rightleftarrows}} CO_2. \tag{13}$$

Here, Eqs. (12) and (13) represent the reactions of the volatile matter and CO, respectively. The reaction rates of these forward reactions, ω_1 and ω_{2f}, are given as

$$\omega_1 = A_1 f_1(\phi) \exp\left(-\frac{E_{a,1}}{RT}\right) [C_aH_bO_c]^{n_{f,1}} [O_2]^{n_{o,1}}, \tag{14}$$

$$\omega_{2f} = A_2 f_2(\phi) \exp\left(-\frac{E_{a,2}}{RT}\right) [CO]^{n_{f,2}} [O_2]^{n_{o,2}}. \tag{15}$$

Here, T is the gas temperature, R the gas constant, and [X] the mole concentration of chemical species X. Also, A_i, $E_{a,i}$, $n_{f,i}$, $n_{o,i}$ are the constants related to reaction rate,

and $f_i(\phi)$ are the correction factor as a function of local equivalence ratio, ϕ. In order to estimate T_b precisely, the reverse reaction of Eq. (13) is considered using equilibrium constant, K_c, as

$$
\begin{aligned}
\omega_{2r} &= A_2 f_2\left(\phi\right) \exp\left(\frac{E_{a,2}}{RT}\right) \frac{1}{K_c}\left[CO_2\right] \\
&= A_2 f_2\left(\phi\right) \exp\left(\frac{E_{a,2}}{RT}\right) C^{-\Delta\nu} \exp\left(\frac{\Delta G^\circ}{RT}\right)\left[CO_2\right],
\end{aligned}
\tag{16}
$$

and finally

$$
\omega_2 = \omega_{2f} - \omega_{2r},
\tag{17}
$$

is obtained. Here, C is the total mole concentration, $\Delta\nu$ the mole number change ($= 1/2$), and ΔG the change in the Gibbs free energy in the reaction ($= \Delta H - T\Delta S$).

The above constants, A_i, $E_{a,i}$, $n_{f,i}$, $n_{o,i}$, and correction factors, $f_1(\phi)$ and $f_2(\phi)$, are adjusted in order to meet the requirements that the values of s_L and T_b should be in good agreement with those obtained using the detailed reaction mechanism not only under the various ϕ, P and T_u conditions, but also under various conditions of dilution by H_2O and CO_2 (see the previous section). $f_1(\phi)$ and $f_2(\phi)$ are given as

$$
f_1\left(\phi\right) = \frac{2}{\left[1 + \tanh\left(\frac{\phi_{0,1}-\phi}{\sigma_{0,1}}\right)\right] + B_1\left[1 + \tanh\left(\frac{\phi-\phi_{1,1}}{\sigma_{1,1}}\right)\right] + C_1\left[1 + \tanh\left(\frac{\phi-\phi_{2,1}}{\sigma_{2,1}}\right)\right]},
\tag{18}
$$

$$
\begin{aligned}
f_2\left(\phi\right) = {}&\frac{1}{2}\left[1 + \tanh\left(\frac{\phi_{0,2}-\phi}{\sigma_{0,2}}\right)\right] + \frac{B_2}{2}\left[1 + \tanh\left(\frac{\phi-\phi_{1,2}}{\sigma_{1,2}}\right)\right] \\
&+ \frac{C_2}{2}\left[1 + \tanh\left(\frac{\phi-\phi_{2,2}}{\sigma_{2,2}}\right)\right] \times \left[1 + \tanh\left(\frac{\phi_{3,2}-\phi}{\sigma_{3,2}}\right)\right].
\end{aligned}
\tag{19}
$$

Here, $\phi_{j,i}$, $\sigma_{j,i}$, B_i, C_i are the constants. In these equations, ϕ is defined by

$$
\phi = \frac{\left(\beta - \beta_{\text{oxidizer}}\right)\beta_{\text{fuel}}}{\left(\beta - \beta_{\text{fuel}}\right)\beta_{\text{oxidizer}}},
\tag{20}
$$

10

$$\beta = 2\frac{Y_{\mathrm{C}}}{W_{\mathrm{C}}} + \frac{1}{2}\frac{Y_{\mathrm{H}}}{W_{\mathrm{H}}} - \frac{Y_{\mathrm{O}}}{W_{\mathrm{O}}}. \tag{21}$$

Here, Y_M and W_M are the mass fraction and molecular weight of element M, respectively. $\beta_{\mathrm{oxidizer}}$ and β_{fuel} are the values for the pure O_2 and volatile matter ($\beta_{\mathrm{fuel}} = (2a + b/2 - c)/W_{\mathrm{C}_a\mathrm{H}_b\mathrm{O}_c}$), respectively.

The values of A_i, $E_{a,i}$, $n_{f,i}$, $n_{o,i}$ in Eqs. (14) and (15) are listed in Table 5 (here, the units used are mol, s, cm^3, J and cal/mol.), and the values of $\phi_{j,i}$, $\sigma_{j,i}$, B_i, C_i in Eqs. (18) and (19) are listed in Table 6.

2.2. Results and Discussion

In order to assess the validity of the proposed two-step reaction scheme together with the models of the properties of the volatile matter, the laminar flame speed, s_L, and burned gas temperature, T_b, are compared with the corresponding values obtained using the detailed reaction mechanism.

Figure 6 shows the comparisons of s_L against equivalence ratio, ϕ, between proposed two-step reaction and detailed reaction at $T_u = 300$, 500 and 700 K (Newlands coal, $P = 0.1$, 0.3 and 1.0 MPa). It is observed that s_L increases with increasing T_u and decreasing P and has peaks around $\phi = 1.1$ for all cases, and that the predicted s_L are in good agreement with those obtain by using the detailed reaction mechanism. This supports the validity of the present model for various equivalence ratio, pressure and unburned gas temperature conditions.

The comparisons of s_L and T_b of volatile matter against equivalence ratio, ϕ, between the proposed two-step reaction and detailed reaction (Newlands, Adaro and Yallourn coals, $T_u = 300$ K, $P = 0.1$ MPa) are shown in Fig. 7. It is found that s_L and T_b of Yallourn coal are smaller than those of Newlands coal. This is because the volatile matter of low-rank coal with low carbon content such as Yallourn coal contains high H_2O and CO_2 content, which reduces the calorific value and then decreases the flame temperature. Further, good agreements between the predicted s_L and T_b and those obtained by the detailed reaction mechanism suggests that present model is capable of capturing the effect of the differences in the coal properties depending on the coal types.

Figure 8 shows the comparison of s_L of volatile matter diluted by H_2O, CO_2, and a mixture of H_2O and CO_2 ($H_2O : CO_2 = 1 : 1$) against dilution rate, DR, between the proposed two-step reaction and detailed reaction (Newlands coal, $\phi = 1.0$). In all cases, s_L is found to decrease with increasing DR. This is attributed to the fact that the fuel ratio in the mixture gas decreases, which reduces the calorific value and increases the thermal capacity [34–36]. It is verified that the predicted s_L are in general agreement with those obtained by the detailed reaction mechanism, and therefore, the present model can simulate the effects of dilution by H_2O and CO_2. Although a difference is observed in the effect of DR induced by CO_2, this is considered due to the fact that the proposed reaction rates associated with the equilibrium reaction between CO_2 and CO are strongly affected by the CO_2 dilution.

3. Direct Numerical Simulation of Pulverized Coal Jet Flame

3.1. Numerical Methods

3.1.1. Gas Phase

The governing equations for the gas phase are the conservation equations of mass, momentum, energy, mass of each chemical species k, and the equation of state for the ideal gas as

$$\frac{\partial \rho}{\partial t} + \nabla \cdot (\rho \boldsymbol{u}) = S_\rho, \tag{22}$$

$$\frac{\partial \rho \boldsymbol{u}}{\partial t} + \nabla \cdot (\rho \boldsymbol{u} \boldsymbol{u}) = -\nabla P + \nabla \cdot \boldsymbol{\sigma} + S_{\rho u}, \tag{23}$$

$$\frac{\partial \rho h}{\partial t} + \nabla \cdot (\rho h \boldsymbol{u}) = \nabla \cdot (\rho D_h \nabla h) + \boldsymbol{\sigma} \cdot \nabla \boldsymbol{u} + q_{\text{rad}} + S_{\rho h}, \tag{24}$$

$$\frac{\partial \rho Y_k}{\partial t} + \nabla \cdot (\rho Y_k \boldsymbol{u}) = \nabla \cdot (\rho D_k \nabla Y_k) + S_{\text{comb},k} + S_{\rho Y_k}, \tag{25}$$

$$P = \rho R T. \tag{26}$$

Here, ρ is the density, $\boldsymbol{u}$ the gas velocity, P the pressure, $\boldsymbol{\sigma}$ the viscous stress tensor, h the specific enthalpy, D_h the diffusion coefficient of enthalpy ($= \lambda/\rho C_p$), Y_k and D_k the mass fraction and the diffusion coefficient of chemical species k, and R the gas constant, respectively. In this study, D_k is given under the unity Lewis number assumption as

$D_k = D_h$. Also, q_{rad} is the source term due to the radiation which is calculated by Discrete Ordinate Method (DOM)/S4 [37] with an absorption coefficient obtained by WSGG (Weighted Sum of Gray Gases) [38], and $S_{\text{comb},k}$ is the source term due to the combustion reaction. As a reaction model of gas phase regarding $S_{\text{comb},k}$, the two-step global reaction scheme for the volatile matter of coal model proposed above (Eqs. (12) and (13)) is used. In addition, CH_4 reaction for the pilot burner is solved by (see below)

$$CH_4 + \left(\frac{3}{2}\right) O_2 \xrightarrow{\omega_3} CO + 2H_2O, \tag{27}$$
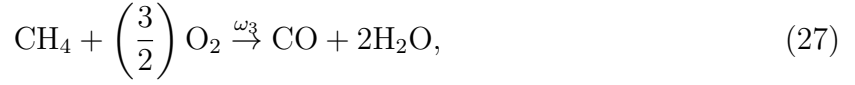
$$\omega_3 = A_3 f_3 (\phi) \exp\left(-\frac{E_{a,3}}{RT}\right) [CH_4]^{n_{f,3}} [CO]^{n_{o,3}}. \tag{28}$$

Here, the coefficients of the reaction rate of CH_4 is the same as those in a previous work by Franzelli $et\ al.$ [29]. S_ρ, $S_{\rho u}$, $S_{\rho h}$ and $S_{\rho Y_k}$ are the source terms attributed to the phase coupling between the gas and dispersed-coal phases calculated by a Particle-Source-In-Cell (PSI-Cell) model [39] described in the next section.

3.1.2. Dispersed Phase (Coal Particles)

For the PSI-Cell method [39], the governing equations for each coal particle's position, x_p, velocity, u_p, temperature, T_p, and mass, m_p, are given by

$$\frac{d\boldsymbol{x}_p}{dt} = \boldsymbol{u}_p, \tag{29}$$

$$\frac{d\boldsymbol{u}_p}{dt} = \frac{g_1}{\tau_p} (\boldsymbol{u} - \boldsymbol{u}_p), \tag{30}$$

$$\frac{dT_p}{dt} = \frac{1}{m_p C_{\text{coal}}} \left(A_p \alpha g_2 (T - T_p) + A_p \varepsilon_p (G - \sigma T_p^4)\right)$$
$$+ \Delta h_{\text{devol},k} \frac{dV_k}{dt} + Q_{\text{char}} \frac{dC}{dt}, \tag{31}$$

$$\frac{dm_p}{dt} = -\sum_k \frac{dV_k}{dt} + \frac{dC}{dt}. \tag{32}$$

Here, τ_p the particle relaxation time $(=\rho_p d_p^2/18\mu$, where ρ_p is the particle density and d_p is the particle diameter), C_{coal} the heat capacity of the coal particle, A_p the surface

area of coal particle, α the heat transfer coefficient between the gas and dispersed-coal phases, σ the Stefan-Boltzmann constant, ε_p the emissivity of particles, Q_{char} the heat source due to char combustion, C the mass of fixed carbon, and $\Delta h_{\text{devol},k}$ and V_k the heat sink due to devolatilization and water evaporation and the mass of chemical species k in volatile matter in coal, respectively. Further, g_1 and g_2 are the correction coefficient of Stokes drag ($g_1 = 1 + 0.15 Re_p^{0.687}$ [40]) and the correction coefficient of heat transfer ($g_2 = z/(e^z - 1)$, $z = -C_p(dm_p/dt)/\pi d_p \lambda (2 + 0.552 Re_p^{1/2} \text{Pr}^{1/3})$, [5, 6, 38]), respectively. For estimating ε_p and C_{coal}, the model of Baum and Street [41] is employed. G is the incident radiation flux computed by $G = \int_{4\pi} I d\Omega$ where Ω is the solid angle.

By using the number of coal particles existing in a volume of computational grid, N_p, the source terms in Eqs. (22) – (25) are given by

$$S_\rho = -\frac{1}{\Delta V} \sum_{N_p} \frac{dm_p}{dt}, \tag{33}$$

$$S_{\rho u} = -\frac{1}{\Delta V} \sum_{N_p} \frac{dm_p \boldsymbol{u}_p}{dt}, \tag{34}$$

$$S_{\rho h} = -\frac{1}{\Delta V} \sum_{N_p} \frac{d}{dt} \sum_{k} m_{p,k} h_{p,k}, \tag{35}$$

$$S_{\rho Y_k} = -\frac{1}{\Delta V} \sum_{N_p} \frac{dm_{p,k}}{dt}. \tag{36}$$

Here, ΔV is the volume of the computational cell, and $m_{p,k}$ and $h_{p,k}$ are the particle mass and the enthalpy of chemical species k, respectively.

The shape of the coal particle is assumed to be spherical, and collision and breakup of particles are not considered. It is also assumed that the change in particle mass leads only to change in density while the particle diameter remains constant. There are previous researches investigating the change of the coal particle diameter, namely swelling and reduction during the devolatilization and the char combustion (e.g., [42, 43]). However, these findings have not been sufficiently generalized and modeled for numerical simulations yet. Therefore, as the first stage, the present DNS is conducted without considering the change of coal particle diameter. Heated coal particles yield the char containing fixed carbon, nitrogen and ash and the volatile matter on thermal decom-

position. The volatile matter is composed of $C_aH_bO_c$ and H_2O and its devolatilization rate is modeled as

$$\frac{dV}{dt} = K_v(V^* - V'), \tag{37}$$

$$K_v = A_v\exp\left(-\frac{E_v}{RT_p}\right). \tag{38}$$

Here, V is the volatile matter mass, and V^* and V' the initial volatile matter content in coal and the volatilized mass released from coal, respectively. Kinematic parameters of frequency factor, A_v, and activation factor, E_v, are separately given by 2.4×10^4 s^{-1} and 3.7×10^4 J/mol, respectively, for $C_aH_bO_c$, and 2.0×10^4 s^{-1} and 3.1×10^4 J/mol, respectively, for H_2O.

The fixed carbon in char starts getting oxidized at the same time as the commencement of devolatilization. The change in the mass of the char associated with the oxidized reaction is estimated by Field model [44] by

$$\frac{dC}{dt} = -\left(\frac{K_cK_d}{K_c + K_d}\right)P_{O_2}\pi d_p^2, \tag{39}$$

$$K_c = A_c\exp\left(-\frac{E_c}{RT_p}\right), \tag{40}$$

$$K_d = \frac{5.06 \times 10^{-7}}{d_p}\left(\frac{T_p + T}{2}\right)^{0.75}, \tag{41}$$

where both the chemical reaction rate and the O_2 diffusion rate to solid surface are considered. Here, C is the char mass, P_{O_2} the partial O_2 pressure, and K_c and K_d the chemical and diffusion rate coefficients, respectively. The values of the kinematic parameters of the frequency factor, A_c, and activation energy, E_c, are 6.0×10^{-3} s/m and 5.0×10^4 J/mol, respectively [3].

3.1.3. Computational Details

Figure 9 shows the schematic diagrams of the computational domain and inlet boundary conditions, and Table 7 shows the inflow conditions. The domain is the same as that used in previous experiment by Hwang *et al.* [16]. From a central pipe of

15

6 mm in inner diameter, air and coal particles are injected at a speed of 6.37 m/s, and from a surrounding annulus of 8 mm in inner diameter, CH_4 is injected for igniting the coal particles. A streamwise velocity of 0.25 m/s is assigned to the surrounding air for numerical stability. Newlands coal whose properties are listed in Table 8 is used. A Rosin-Rammler distribution with a number-averaged diameter of 25 μm and a mass-averaged diameter of 33 μm is adopted as the coal particle diameter distribution. Figure 10 shows the probability density function for the initial coal-particle diameter.

As the boundary conditions, a slip condition is imposed for the $y-$ and $z-$directions, and a convective outflow condition is imposed in the $x-$direction. A parabolic distribution with an artificial turbulence proposed by Klein *et al.* [45] is adopted for the inlet velocity of the central pipe so that the predicted turbulent intensity corresponds to the experimental value [16] at $x = 60$ mm (the specific length scale in the model is 1 mm). A non-uniform staggered grid is used for computation and the number of grids for $x-$, $y-$ and $z-$directions are 1632, 320, 320, respectively. The grid size at the center of the jet on the inlet for $x-$, $y-$ and $z-$directions are $\Delta x = 120$ μm, $\Delta y = \Delta z = 100$ μm. Here, 75 grids are inserted in the region where the reactions of volatile matter and CO actively occur in the radial direction. The spatial derivatives of the momentum equation are approximated by a fourth-order accurate central difference scheme. For the convection terms of energy and mass fractions of chemical species, a QUICK scheme is employed. A second-order accurate central difference scheme is used for the other terms. The fractional-step method for compressible flows is used as the computational algorithm [8–11], and a third-order explicit Runge-Kutta method is used for the time-advancement computation of the convection terms.

The DNS was performed using the thermal flow analysis code: an in-house code referred to as FK^3. Courant number was kept constant at 0.1 so that the time step was not constant but approximately 10^{-6} s/step. The computation was carried out for 50,000 steps without coal particle to develop the flow field and for 300,000 steps with injection of coal particles. The CPU time for each case was about 400,000 h by a parallel computation using 1,024 cores on SGI:ICEX.

3.2. Results and Discussion

3.2.1. Comparisons with Experiment

Figure 11 shows the instantaneous distributions ($x - y$ plane) of gas temperature, T, and mass fraction of volatile matter, $Y_{C_aH_bO_c}$. It is observed that high gas temperature regions are formed annularly, and high volatile matter concentration regions are distributed inside the high gas temperature regions due to the high devolatilization rate of coal. Also, as the turbulent fluctuation is enhanced toward the downstream, high volatile matter concentration regions become to be observed in spots in the central low gas temperature region. This is considered to be due to the fact that the volatile matter, which is formed near the high gas temperature regions and transported inward, remains because of the low reactivity owing to the low gas temperature.

Figure 12 shows the comparisons of streamwise profiles of mean streamwise particle velocity, $\overline{U_p}$, and root mean square of streamwise particle velocity fluctuation, u'_p, on the central axis among the present DNS, the existing LES performed by Franchetti *et al.* [46] and the experiment using both Shadow Doppler Particle Analyzer (SDPA) and Laser Doppler Velocimetry (LDV) [16]. It is found that for the present DNS, the predicted $\overline{U_p}$ decreases with x and the predicted u' peaks at around $x = 0.04$ m and then decreases with x, and that these values agree well quantitatively with those obtained in the experiment [16]. Further, for both $\overline{U_p}$ and u', the present DNS gives better agreements with the experiment than the existing LES [46].

Figure 13 shows the comparisons of radial profiles of $\overline{U_p}$ and u'_p at two different positions among the present DNS, the existing LES [46] and the experiment [16]. There appear some discrepancies in both $\overline{U_p}$ and u'_p. For $\overline{U_p}$, the profiles predicted by the DNS are observed to be lower than those in the experiment as a whole. This is considered to be due to the fact that the additional air aspirated from the pulverized-coal feeder into the main flow is not considered in the present DNS, although the air supply rate to the burner in the simulations was adjusted in some previous studies (e.g., [6, 11]) in order to take into account this additional air supply. Also, the reason why u'_p in the experiment [16] is larger than that by the DNS in the outer region of $r > 7$ mm at $x = 60$ mm is considered to be due to the gravity. The gravity effect is not considered

17

in the present DNS so that dispersions of the coal particles are tempered compared to the experiment [16] in this region.

The comparison of instantaneous coal particle distribution ($x - y$ plane) between the present DNS and the experiment employing Mie scattering [16] is shown in Fig. 14. In Fig. 14 (a), only the coal particles in the region $|z| \leq 0.001$ m are shown. The predicted spatial number density pattern of the coal particles is similar to that in the experiment [16]. This behavior is discussed in more detail later.

Figure 15 shows the comparison among particle temperatures by the present DNS and experiment using a two-color radiation pyrometer [16], and maximum gas temperature by the present DNS. The DNS plots are colored by the distance of the coal particles from the central axis. The predicted gas and particle temperatures at the central axis are found to generally indicate the larger and lower values than the measured particle temperature, respectively. These discrepancies are attributed to the fact that the coal particle temperature obtained using the two-color radiation pyrometer is not the particle temperature at a local point and is affected by the temperatures of coal particles, gas and soot in the whole pulverized coal flame [16].

In Fig. 16, comparisons among the present DNS, the existing LES [46] and the experiment [16] for mean O_2 and CO_2 concentrations (mole fractions) on the central axis are shown. For both O_2 and CO_2 concentrations, the present DNS gives better agreements with the experiment than the existing LES [46]. The underestimation in CO_2 concentration in the present DNS is considered due to the facts that in the experiment [16], the spatial resolution of the suction sampling method is so large that the reaction product gas in the outer flame is not a little sucked and a portion of CO is converted to CO_2 during sampling. It is predicted that the precise measurement of the CO_2 concentration increases the O_2 concentration, which enlarges the difference in the O_2 concentration between the present DNS and the experiment [16]. However, this discrepancy is considered to be reduced by taking into account the additional air aspirated from the pulverized-coal feeder into the main flow, as described above. On the other hand, the underestimation in O_2 and overestimation in CO_2 concentrations in the LES [46] compared to the experiment [16] are considered due to the fact that in

the LES [46], Eddy Break Up model which cannot consider the finite rate chemistry is used for the estimation of the chemical reaction rate. This also may result in the overestimation and underestimation in $\overline{U_p}$ in the upstream region at around $x = 0.05$ m and in the downstream region beyond $x = 0.1$ m in the LES [46], respectively, as shown in Fig. 12. In this regard, the prediction accuracy is improved in the present DNS.

Based on the above results, it can be said that the present DNS with the proposed reaction scheme of the volatile matter succeeds in capturing the general behavior of pulverized coal combustion.

3.2.2. Coal Particle Behavior

In order to examine the effect of particle size on the spatial distribution of particles, the instantaneous coal particle distributions ($x - y$ plane) and Stokes number, St, of all particle of diameters in the ranges $10 - 18.5$ μm, $21.5 - 26$ μm and $31 - 40$ μm are shown in Fig. 17. Here, St is defined as

$$St = \frac{\tau_p}{\tau_K} = \frac{\rho_p d_p^2 / 18 \rho \nu}{(\nu / \epsilon)^{1/2}}. \tag{42}$$

Here, τ_p is the particle relaxation time, τ_K the Kolmogorov time scale, and ε the energy dissipation rate. In the figure, only the coal particles in the region $|z| \leq 0.001$ m are shown, and the color of the particle indicates the value of St. It is observed that the particles with $St = 1$ exist in the upstream region in the case of small particles, whereas they exist in the downstream region in the case of larger particles. Further, the spatial number density pattern of the coal particles tends to become evident for the particles around with $St = 1$. This is due to the fact that these particles tend to show the preferential concentration owing to the effect of turbulence [47]. The reason why the region of particles with $St = 1$ shifts downstream with increasing particle size is that the initial St of small particles are around unity, whereas St of large particles decreases to unity downstream as τ_p decreases owing to the devolatilization and τ_K increases owing to the turbulence decay.

19

3.2.3. Combustion Behavior

The combustion characteristics in the pulverized coal flame are investigated by using flame index, F.I., which is a useful diagnostic tool for investigating the flame structure [48] and was applied to spray flames recently [49–51]. The value of the flame index is obtained by multiplying the spatial gradients of fuel and oxidizer mass fractions as

$$\text{F.I.} = \nabla Y_f \cdot \nabla Y_{\text{O}_2}, \tag{43}$$

where Y_f $(= Y_{\text{C}_a\text{H}_b\text{O}_c} + Y_{\text{CO}})$ and Y_{O_2} are the mass fractions of the fuel and oxidizer, respectively. The flame index is used to distinguish premixed and diffusion flames, respectively indicated by positive and negative values of F.I. Here, $Y_f = Y_{\text{C}_a\text{H}_b\text{O}_c} + Y_{\text{CO}}$. Figure 18 shows the instantaneous distribution $(x - y$ plane) of F.I. In this figure, in order to avoid an incorrect diagnosis of F.I. caused by the high devolatilization rate of coal (i.e., F.I. incorrectly indicates the diffusion flame, see [49]), only the regions where the decreasing rate of the O_2 mass fraction attribute to the reaction exceeds 0.05 s^{-1} are shown. There appear three flame layers indicating the diffusion (F.I. $<$ 0), premixed (F.I. $>$ 0) and diffusion (F.I. $<$ 0) flames from the inner to outer regions in the flame.

In order to understand which reaction occurs in each layer, the spanwise profiles of instantaneous mass fractions of $\text{C}_a\text{H}_b\text{O}_c$, O_2, CO_2 and CO and reaction rates of $\text{C}_a\text{H}_b\text{O}_c$ and CO, ω_1 and ω_2, at $x = 60$ mm and 120 mm are shown in Figs. 19 and 20, respectively. At both streamwise distances, both $\text{C}_a\text{H}_b\text{O}_c$ and O_2 decrease with y and ω_1 has a peak (as indicated by arrow (i)) in the second inner layer, indicating the premixed flame, whereas CO decreases and O_2 increases with y and ω_1 and ω_2 have peaks (as indicated by arrow (ii)) in the outermost layer, indicating the diffusion flame. This shows that the reaction of the volatile matter and O_2 in coal-carrier air occurs in the inner premixed flame layer, whereas the reactions of the volatile matter and CO and O_2 in surrounding air occur in the outer diffusion flame layer. In the innermost layer, indicating the diffusion flame in Fig. 18, on the other hand, a high reaction rate is not observed.

In order to explain F.I. < 0 in the innermost layer, Fig. 21 shows the instantaneous distributions ($x - y$ plane) of the normalized devolatilization rate for each particle, $\frac{1}{V^\star}\frac{dV}{dt}$, and F.I. Here, in the figure, only the coal particles in the region $|z| \leq 0.001$ m are shown, and the color of the particle indicates the value of $\frac{1}{V^\star}\frac{dV}{dt}$. Again, only the regions where the decreasing rate of the O_2 mass fraction attribute to the reaction exceeds 0.05 s^{-1} are shown. The volatile matter is found to be drastically released from coal in this innermost layer, indicating the diffusion layer (F.I. < 0). Therefore, it is considered that although the regions corresponding to a low-consumption rate of O_2 are eliminated, the production rate of the volatile matter by devoatilization exceeds its consumption rate in the reaction (premixed combustion), which increases $Y_{C_a H_b O_c}$ with y and makes F.I. negative.

4. Conclusions

In this study, a precise two-step global reaction scheme for the volatile matter of coal was proposed, and the unsteady coal particle and combustion behaviors in a turbulent pulverized coal jet flame were investigated by performing DNS employing the proposed global reaction scheme. The main results obtained in this study are as follows.

1. The proposed two-step global reaction scheme for the volatile matter of coal can precisely predict the laminar flame speed and burned gas temperature for various coal types from bituminous to low-rank coals over wide ranges of conditions of equivalence ratios [0.6; 1.8], pressures [0.1; 1.0] MPa and unburned gas temperatures [300; 700] K. In addition, it can correctly take into account the effects of dilutions by H_2O and CO_2 which compromise the evaporated moisture from coal and products of char reaction.

2. A lab-scale turbulent pulverized coal jet flame is well predicted by the DNS employing the proposed global reaction scheme. The pulverized coal particles velocity and its fluctuation, the characteristics of particle preferential motion and the chemical species concentrations are in general agreement with those observed in the experiment.

3. In the turbulent pulverized coal jet flame, there appear premix and diffusion flame layers inside and outside, respectively. The reaction of the volatile matter and O_2 in coal-carrier air occurs in the inner premixed flame layer, whereas the reactions of the volatile matter and CO and O_2 in surrounding air occur in the outer diffusion flame layer.

References

[1] R. Kurose, M. Ikeda, H. Makino, Fuel, **80** (2001) 1447–1455.

[2] R. Kurose, H. Tsuji, H. Makino, Fuel, **80** (2001) 1457–1465.

[3] R. Kurose, M. Ikeda, H. Makino, M. Kimoto, T. Miyazaki, Fuel, **83** (2004) 1777–1785.

[4] R. Kurose, H. Watanabe, H. Makino, KONA Powder Part. J., **27** (2009) 144–156.

[5] N. Hashimoto, R. Kurose, S.-M. Hwang, H. Tsuji, H. Shirai, Combust. Flame, **159** (2012) 353–366.

[6] N. Hashimoto, R. Kurose, H. Shirai, Fuel, **97** (2012) 277–287.

[7] A. H. Al-Abbas, J. Naser, E. K. Hussein, Fuel, **107** (2013) 688–698.

[8] R. Kurose, H. Makino, Combust. Flame, **135** (2003) 1–16.

[9] K. Yamamoto, T. Murota, T. Okazaki, M. Taniguchi, Proc. Combust. Inst., **33** (2011) 1771–1778.

[10] L. Chen, A. F. Ghoniem, Energy Fuels, **26** (2012) 4783–4798.

[11] O. Stein, G. Olenik, A. Kronenburg, F. C. Marincola, B. Franchetti, A. Kempf, M. Ghiani, M. Vascellari, C. Hasse, Flow Turb. Combust., **90** (2013) 859–884.

[12] G. Olenik, O. Stein, A. Kronenburg, Proc. Combust. Inst., **35** (2015) 2819–2828.

[13] M. Muto, H. Watanabe, R. Kurose, S. Komori, S. Balusamy, S. Hochgreb, Fuel, **142** (2015) 152–163.

[14] M. Rabacal, B. Franchetti, F. C. Marincola, F. Proch, M. Costa, C. Hasse, A. Kempf, Proc. Combust. Inst., **35** (2015) 3609–3617.

[15] K. Luo, H. Wang, J. Fan, F. Yi, Energy Fuels, **26** (2012) 6128–6136.

[16] S. M. Hwang, R. Kurose, F. Akamatsu, H. Tsuji, H. Makino, M. Katsuki, Energy Fuels, **19** (2005) 382–392.

[17] W. C. Xu, A. Tomita, Fuel, **66** (1987) 627–631.

[18] D. M. Grant, R. J. Pugmire, T. H. Fletcher, A. R. Kerstein, Energy Fuels, **3** (1989) 175–186.

[19] P. Solomon, D. Hamblen, R. Carangelo, M. Serio, G. Deshpande, Energy Fuels, **2** (1988) 405–422.

[20] S. Niksa, A. R. Kerstein, Energy Fuels, **5** (1991) 647–665.

[21] D. Van Krevelen, Fuel, **29** (1950) 269–284.

[22] D. Genetti, T. H. Fletcher, R. J. Pugmire, Energy Fuels, **13** (1999) 60–68.

[23] H. Pitsch, M. Bollig, Flamemaster, a computer code for homogeneous and one-dimensional laminar flame calculations, Institut für Technische Mechanik, RWTH Aachen, 1994.

[24] K. Narayanaswamy, G. Blanquart, H. Pitsch, Combust. Flame, **157** (2010) 1879–1898.

[25] S. Gordon, B. J. McBride, Technical Report NASA SP-273, 1976.

[26] R. J. Kee, F. M. Rupley, E. Meeks, J. A. Miller, Sandia National Laboratories Report SAND96-8216, 1996.

[27] R. J. Kee, G. Dixon-Lewis, J. Warnatz, M. E. Coltrin, J. A. Miller, Sandia National Laboratories Report SAND86-8246B, 1986.

[28] B. Franzelli, E. Riber, M. Sanjosé, T. Poinsot, Combust. Flame, **157** (2010) 1364–1373.

[29] B. Franzelli, E. Riber, L. Y. Gicquel, T. Poinsot, Combust. Flame, **159** (2012) 621–637.

[30] S. Hermeth, G. Staffelbach, L. Y. Gicquel, T. Poinsot, Proc. Combust. Inst., **34** (2013) 3165–3173.

[31] A. G. Smith, S. Menon, J. A. Lovett, B. A. Sen, J. Eng. Gas Turbines Power, **136** (2014) 031505.

[32] E. Motheau, F. Nicoud, T. Poinsot, J. Fluid Mech., **749** (2014) 542–576.

[33] M. Philip, M. Boileau, R. Vicquelin, E. Riber, T. Schmitt, B. Cuenot, D. Durox, S. Candel, Proc. Combust. Inst., **35** (2015) 3159–3166.

[34] B. Galmiche, F. Halter, F. Foucher, P. Dagaut, Energy Fuels, **25** (2011) 948–954.

[35] A. Mazas, D. Lacoste, T. Schuller, ASME Turbo Expo 2010: Power for Land, Sea, and Air (2010) 411–421.

[36] A. Mazas, B. Fiorina, D. Lacoste, T. Schuller, Combust. Flame, **158** (2011) 2428–2440.

[37] W. Fiveland, J. Heat Transfer, **106** (1984) 699–706.

[38] T. Smith, Z. Shen, J. Friedman, J. Heat Transfer, **104** (1982) 602–608.

[39] C. T. Crowe, M. Sharma, D. E. Stock, J. Fluids Eng., **99** (1977) 325–332.

[40] L. Schiller, A. Naumann, Z. Ver. Dtsch. Ing, **77** (1933) 318–320.

[41] M. Baum, P. Street, Combust. Sci. Technol., **3** (1971) 231–243.

[42] R. Kurose, H. Matsuda, H. Makino, A. Suzuki, Advanced Powder Technology, **14** (2003) 673–694.

[43] H. Yang, S. Li, T. H. Fletcher, M. Dong, Energy & Fuels, **28** (2014) 7216–7226.

[44] M. A. Field, Combust. Flame, **13** (1969) 237–252.

[45] M. Klein, A. Sadiki, J. Janicka, J. Comput. Phys., **186** (2003) 652–665.

[46] B. Franchetti, F. C. Marincola, S. Navarro-Martinez, A. Kempf, Proceedings of the Combustion Institute, **34** (2013) 2419–2426.

[47] K. D. Squires, J. K. Eaton, Phys. Fluids A, **3** (1991) 1169–1178.

[48] H. Yamashita, M. Shimada, T. Takeno, Symp. (Int.) Combust., **26** (1996) 27–34.

[49] M. Nakamura, F. Akamatsu, R. Kurose, M. Katsuki, Phys. Fluids, **17** (2005) 123301.

[50] H. Watanabe, R. Kurose, S.-M. Hwang, F. Akamatsu, Combustion and Flame, **148** (2007) 234–248.

[51] Y. Baba, R. Kurose, Journal of Fluid Mechanics, **612** (2008) 45–79.

Table 1: Coal properties considered for heat decomposition simulation.

Coal Name	Code	Moisture^a	Ash^b	Proximate analysis (wt %) Volatile Matter^b	Fixed Carbon^b	C	H	Ultimate analysis^c (wt %) N	S	O
Yallourn	(YL)	15.0	1.2	53.3	45.5	65.4	4.9	0.6	0.3	28.8
Rhein Braun	(RB)	20.3	2.9	54.8	42.3	65.8	5.5	0.8	0.3	27.6
Morwell	(MW)	19.6	2.0	51.5	46.5	67.4	5.0	0.5	0.3	26.8
Velva	(VL)	15.8	8.8	47.7	43.5	69.1	4.8	1.4	0.6	23.9
Soyakoishi	(SY)	17.7	10.0	41.8	48.2	70.2	5.2	1.8	0.2	22.4
Adaro	(AD)	20.0	1.2	50.3	48.5	71.6	5.3	1.0	0.1	22.1
South Beulah	(SB)	18.1	13.7	38.6	47.7	71.8	4.7	1.4	2.9	19.2
Colowyo	(CW)	13.2	6.3	36.3	57.4	74.0	5.0	1.9	0.4	18.6
Taiheiyo	(TH)	4.4	12.2	49.2	38.6	76.0	6.5	1.2	0.3	16.0
Millmerran	(MM)	6.6	16.4	45.8	37.8	76.9	6.6	0.5	0.6	15.4
Wandoan	(WD)	10.4	8.3	45.6	46.1	78.5	5.8	0.9	0.4	14.4
Hunter Valley	(HV)	4.4	9.4	33.7	56.9	80.3	5.0	2.0	0.4	12.2
Liddell	(LD)	3.7	8.0	34.6	57.4	83.5	5.4	2.1	0.6	8.4
Newvale	(NV)	3.3	14.4	29.3	56.3	84.2	5.0	1.4	0.5	8.9
Newlands	(NL)	2.6	15.2	26.9	57.9	84.8	5.2	1.8	0.5	7.7
Yubari Shinko	(YS)	1.1	5.2	38.4	56.4	86.9	5.6	1.9	0.3	5.2

^{a} As recieved. ^{b} Dry basis. ^{c} Dry ash free basis.

Table 2: Coefficients of NASA polynomials in Eq. (7).

	$a_{i,\mathrm{refL}}$	$a_{i,\mathrm{refH}}$
	$T \in [300; 1000]$ K	$T \in [1000; 3000]$ K
$a_{1,\mathrm{ref}}$	$1.43163 \times 10^{+0}$	$1.87224 \times 10^{+0}$
$a_{2,\mathrm{ref}}$	1.51366×10^{-2}	1.64883×10^{-2}
$a_{3,\mathrm{ref}}$	3.96599×10^{-7}	-8.75523×10^{-6}
$a_{4,\mathrm{ref}}$	-1.04495×10^{-8}	2.31750×10^{-9}
$a_{5,\mathrm{ref}}$	5.16569×10^{-12}	-2.41847×10^{-13}
$a_{6,\mathrm{ref}}$	$-9.61083 \times 10^{+3}$	Eq. (8)
$a_{7,\mathrm{ref}}$	$1.23064 \times 10^{+1}$	Eq. (9)

Table 3: Coefficients of thermal conductivity and viscosity polynomials in Eq. (10). Units are cm, g, s, K.

$d_{1,\text{ref}}$	$3.81989 \times 10^{+0}$
$d_{2,\text{ref}}$	-3.40355×10^{-1}
$d_{3,\text{ref}}$	2.97977×10^{-1}
$d_{4,\text{ref}}$	-1.88331×10^{-2}
$e_{1,\text{ref}}$	$-1.65067 \times 10^{+1}$
$e_{2,\text{ref}}$	$1.55017 \times 10^{+0}$
$e_{3,\text{ref}}$	-3.94450×10^{-2}
$e_{4,\text{ref}}$	-1.43664×10^{-3}

Table 4: Coefficients of functions in Eqs. (6), (7) and (10).

	f_W	f_{ai} ($i=1,2,\cdots,5$)	$f_{a6\mathrm{L}}$	$f_{a7\mathrm{L}}$	f_d	f_e
$\xi_{X,1}$	$1.83000 \times 10^{+0}$	$1.49936 \times 10^{+0}$	$-2.98764 \times 10^{+0}$	$3.76537 \times 10^{+0}$	$1.15445 \times 10^{+0}$	$1.23036 \times 10^{+0}$
$\xi_{X,2}$	-4.46286×10^{-1}	-5.37764×10^{-2}	$3.15996 \times 10^{+0}$	$-1.91539 \times 10^{+0}$	-2.71250×10^{-1}	-3.26119×10^{-1}
$\xi_{X,3}$	$-1.33857 \times 10^{+0}$	$-2.16464 \times 10^{+0}$	$8.32914 \times 10^{+0}$	$-3.17504 \times 10^{+0}$	5.96030×10^{-1}	-6.14346×10^{-1}
$\xi_{X,4}$	-9.14666×10^{-3}	-7.53927×10^{-2}	-6.78060×10^{-1}	2.47391×10^{-1}	7.70000×10^{-2}	1.65497×10^{-1}
$\xi_{X,5}$	3.53429×10^{-1}	7.96512×10^{-1}	$-2.04629 \times 10^{+0}$	8.75270×10^{-1}	-2.20240×10^{-1}	6.55514×10^{-1}
$\xi_{X,6}$	4.80857×10^{-1}	5.38050×10^{-1}	$-2.76309 \times 10^{+0}$	9.40714×10^{-1}	-2.30100×10^{-2}	-1.53577×10^{-1}

Table 5: Coefficients of reaction rate formula (Eqs. (14) and (15)). Units are mol, s, cm^3, J and cal/mol.

	$E_{a,j}$ [cal/mol]	A_j	$n_{f,j}$	$n_{o,j}$
$j = 1$	3.78×10^4	4.9×10^9	1.0	0.44
$j = 2$	1.80×10^4	2.5×10^9	1.0	0.50

Table 6: Coefficients of correction function, $f_1(\phi)$ and $f_2(\phi)$, in the reaction rate formula (Eqs. (18) and (19)).

	$\phi_{0,j}$	$\sigma_{0,j}$	B_j	$\phi_{1,j}$	$\sigma_{1,j}$	C_j	$\phi_{2,j}$	$\sigma_{2,j}$	$\phi_{3,j}$	$\sigma_{3,j}$
$j = 1$	1.16	0.18	0.5	1.2	0.12	9.5	1.65	0.15	–	–
$j = 2$	1	0.26	0.0002	1.7	0.1	0.25	1.6	0.1	1.3	0.15

Table 7: Inflow conditions [16].

Primary jet	
Air flow rate	1.80×10^{-4} m^3/s
Jet Reynolds number	2544
Pulverized coal feed rate	1.49×10^{-4} kg/s
Bulk equivalence ratio	6.09
Thermal input of coal	4.19 kW
Secondary flow	
CH$_4$ flow rate	2.33×10^{-5} m^3/s
Thermal input of CH$_4$	0.83 kW

Table 8: Properties of Newlands coal [16].

High heating value	29.1 MJ/kg
Low heating value	28.1 MJ/kg
Proximate analysis (wt %)	
Moisture[a]	2.60
Ash[b]	15.20
Volatile matter[b]	26.90
Fixed carbon[b]	57.90
Ultimate analysis[b] (wt %)	
Carbon	71.90
Hydrogen	4.40
Nitrogen	1.50
Oxygen	6.53
Combustable sulfur	0.39

[a] As recieved. [b] Dry basis.
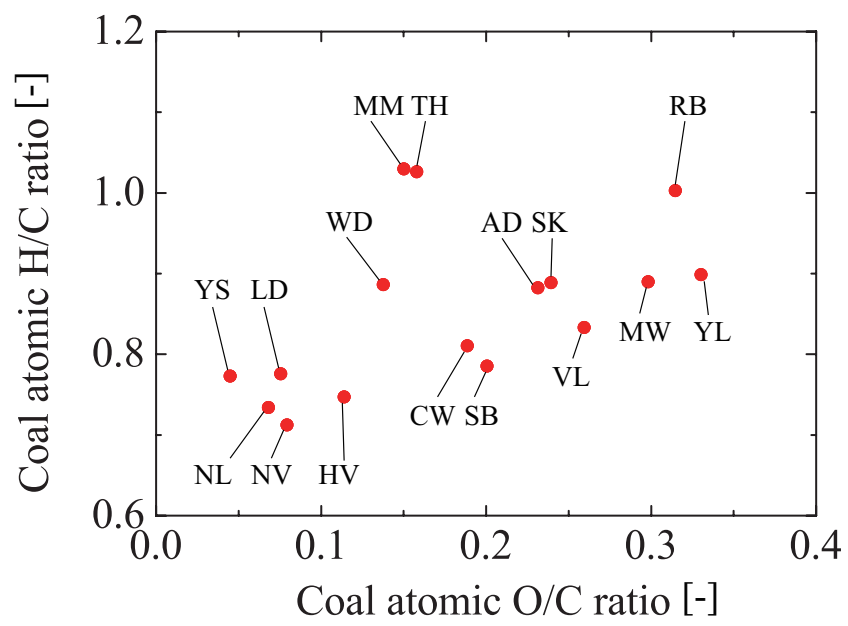
Figure 1: Coal atomic H/C ratio versus coal atomic O/C ratio (van Krevelen diagram [21]).
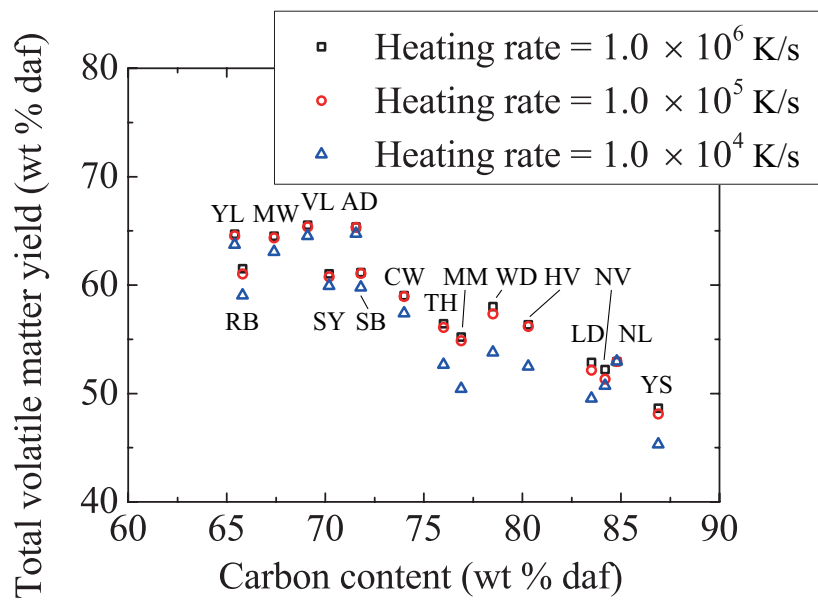
Figure 2: Effects of carbon content and heating rate on volatile matter yield in coal.
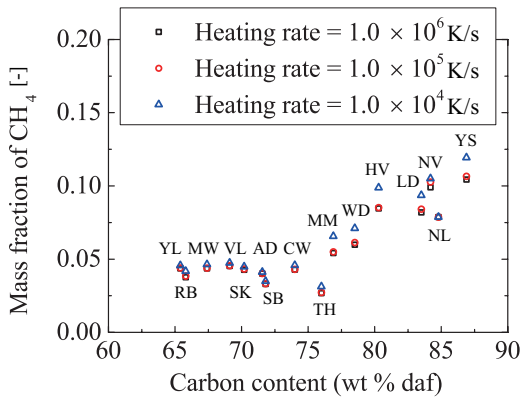
(a)
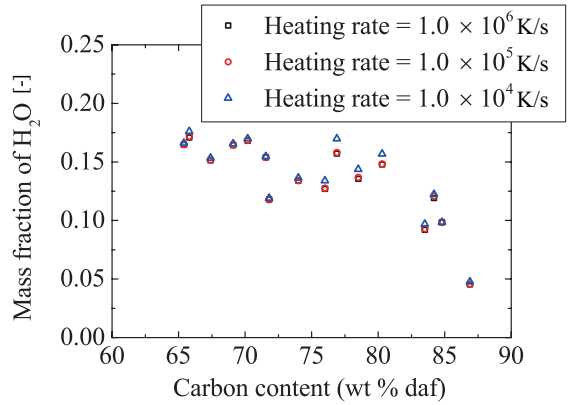
(b)
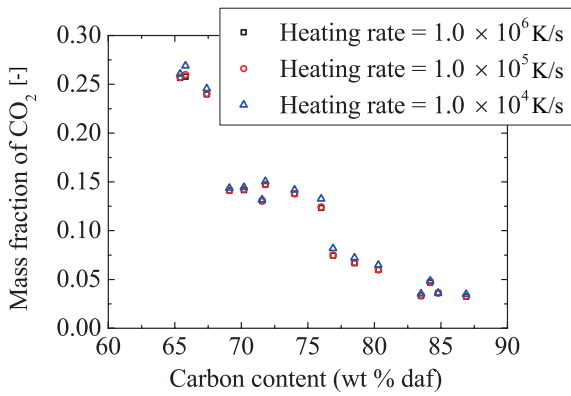
(c)
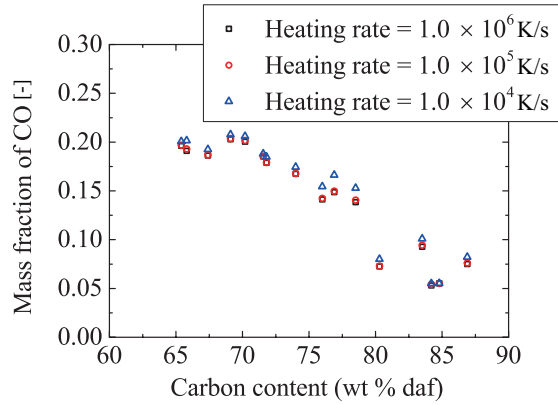
(d)

Figure 3: Effects of carbon content and heating rate on mass fraction of (a) CH_4, (b) H_2O, (c) CO_2, (d) CO, (e) Tar (C_6H_6), (f) H_2, (g) C_2H_6, C_2H_4 and C_3H_6 and (h) C_3H_8 in volatile matter (continued on next page).
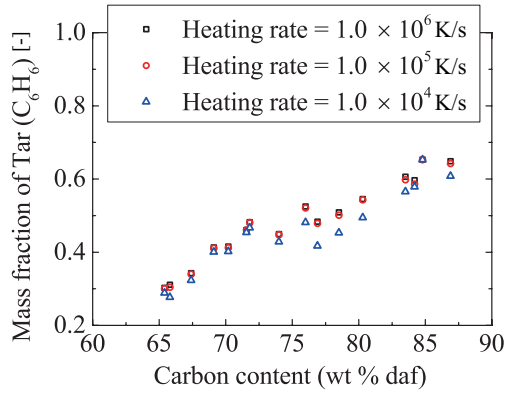
(e)
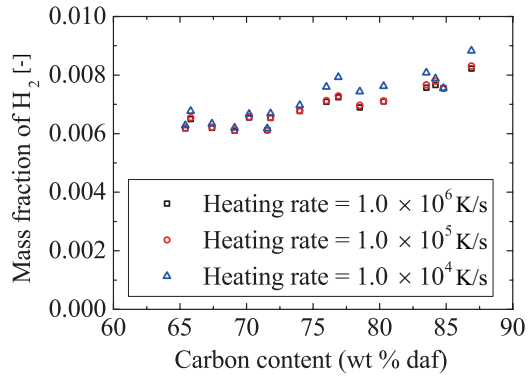
(f)
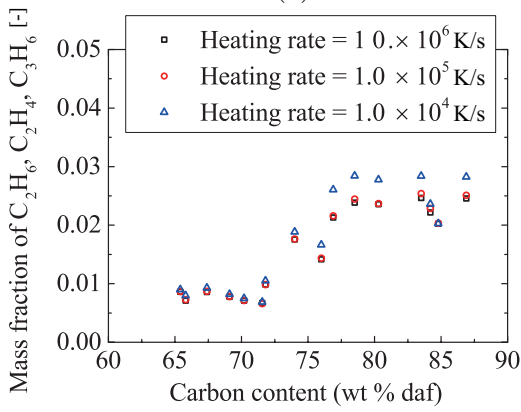
(g)
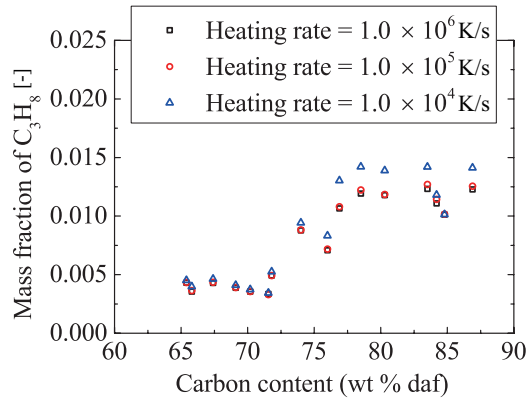
(h)

Figure 3: Effects of carbon content and heating rate on mass fraction of (a) CH_4, (b) H_2O, (c) CO_2, (d) CO, (e) Tar (C_6H_6), (f) H_2, (g) C_2H_6, C_2H_4 and C_3H_6 and (h) C_3H_8 in volatile matter (continued from previous page).
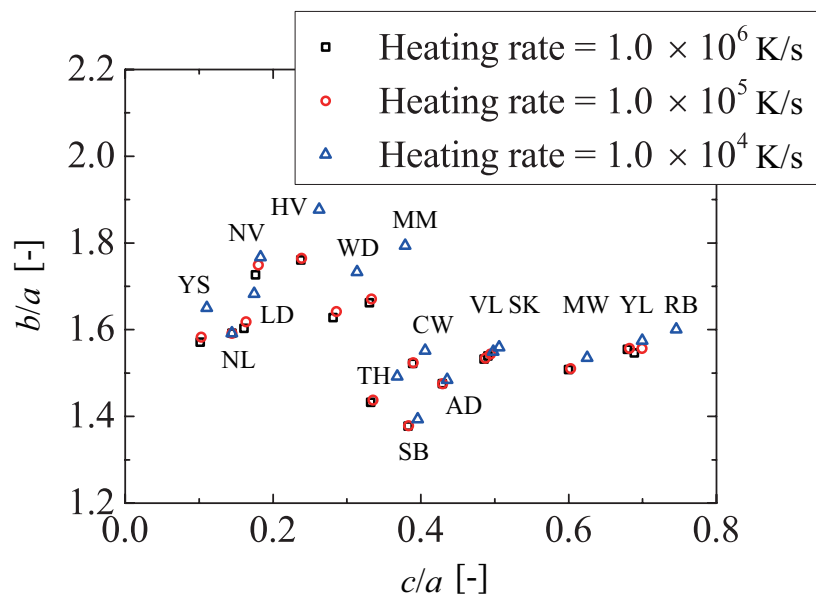
Figure 4: Volatile matter atomic H/C ratio (b/a) versus volatile matter atomic O/C ratio (c/a).
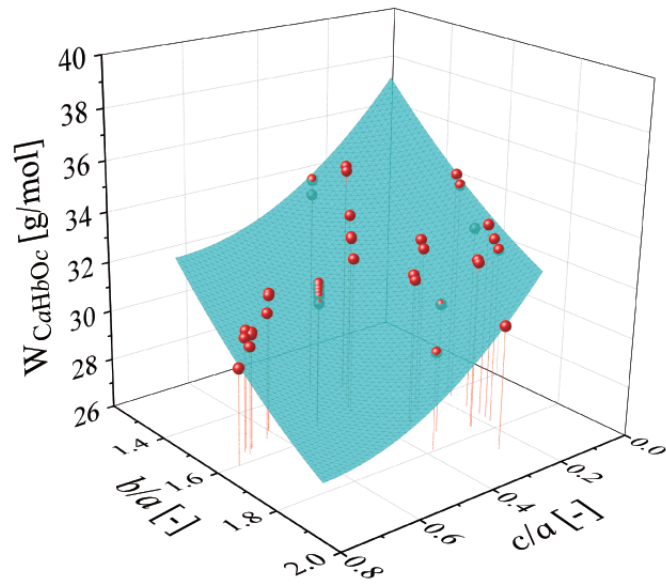
(a)
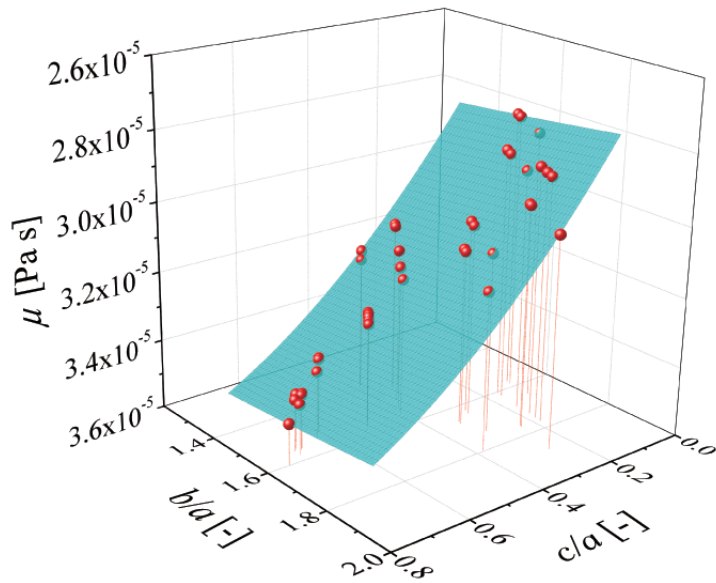
(b)

Figure 5: Effects of volatile matter compositions (b/a and c/a) on (a) molecular weight, $W_{C_a H_b O_c}$, (b) viscosity, μ, and (c) thermal conductivity, λ. A curved surface and red plots show the values obtained by proposed model and CHEMKIN [26, 27], respectively (continued on next page).
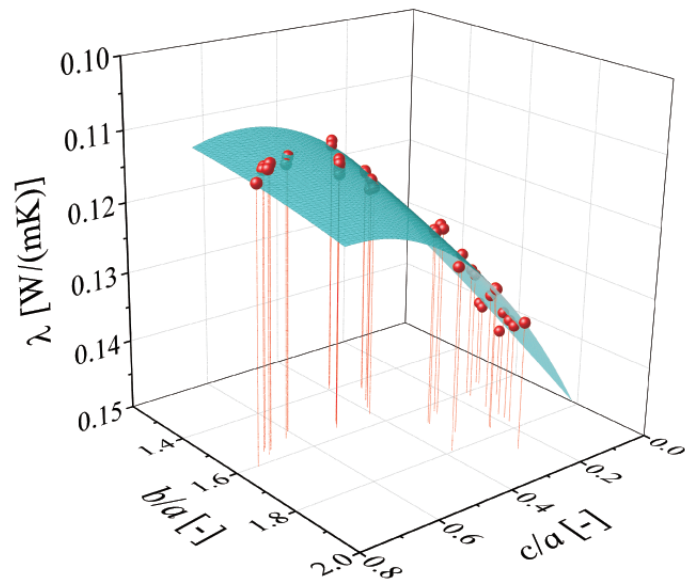
(c)

Figure 5: Effects of volatile matter compositions (b/a and c/a) on (a) molecular weight, $W_{C_aH_bO_c}$, (b) viscosity, μ, and (c) thermal conductivity, λ. A curved surface and red plots show the values obtained by proposed model and CHEMKIN [26, 27], respectively (continued from previous page).
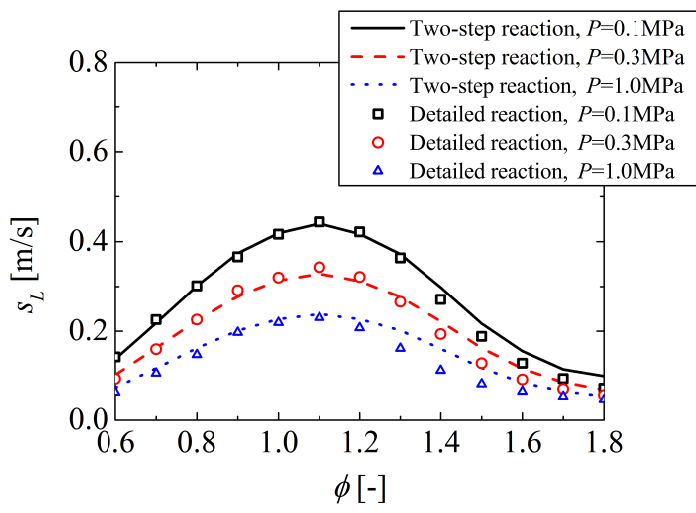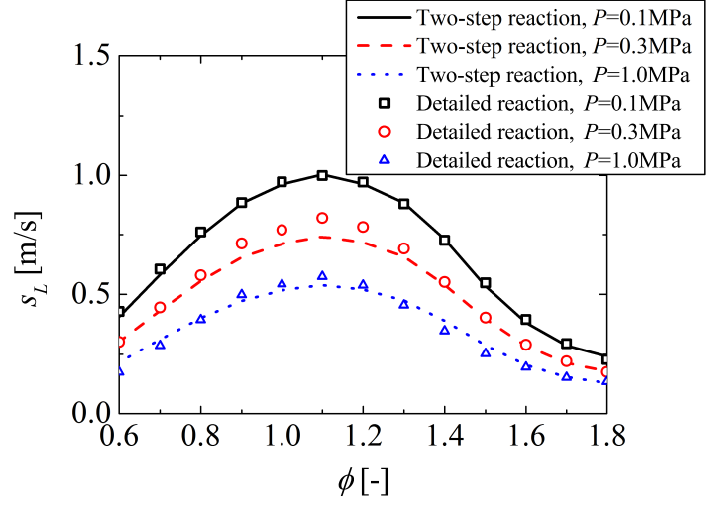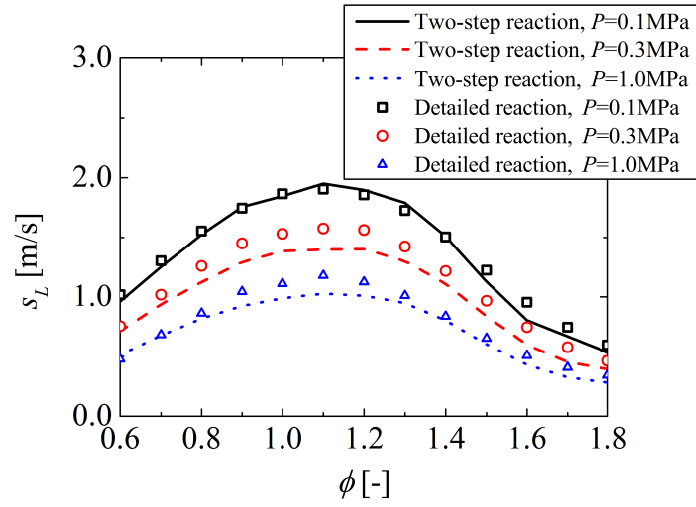
Figure 6: Comparisons of laminar flame speed, s_L, of volatile matter against equivalence ratio, ϕ, between proposed two-step reaction and detailed reaction at T_u = (a) 300 K, (b) 500 K and (c) 700 K (Newlands coal, P =0.1, 0.3 and 1.0 MPa).
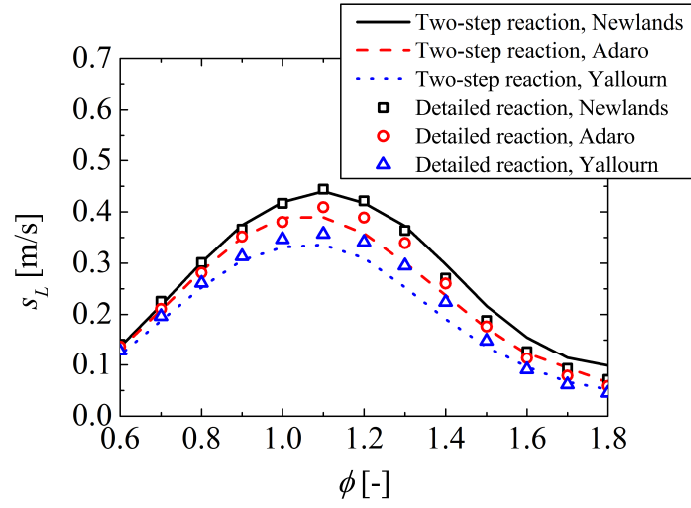
(a)
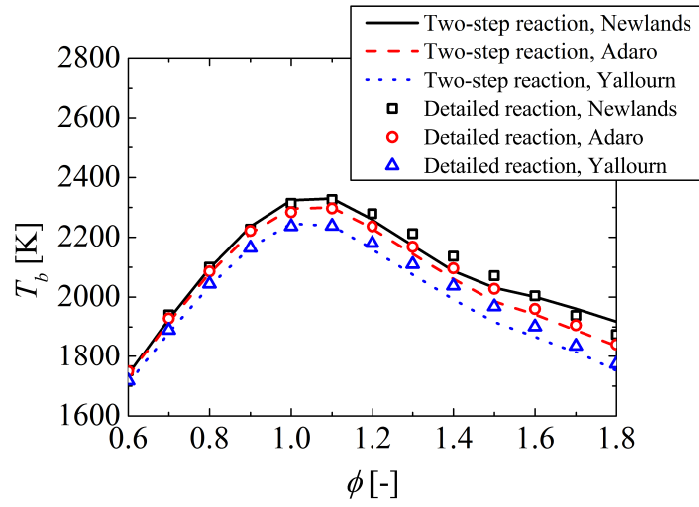
(b)

Figure 7: Comparisons of (a) laminar flame speed, s_L, and (b) burnt gas temperature, T_b, of volatile matter against equivalence ratio, ϕ, between proposed two-step reaction and detailed reaction (Newlands, Adaro and Yallourn coals, $T_u = 300$ K, $P = 0.1$ MPa).
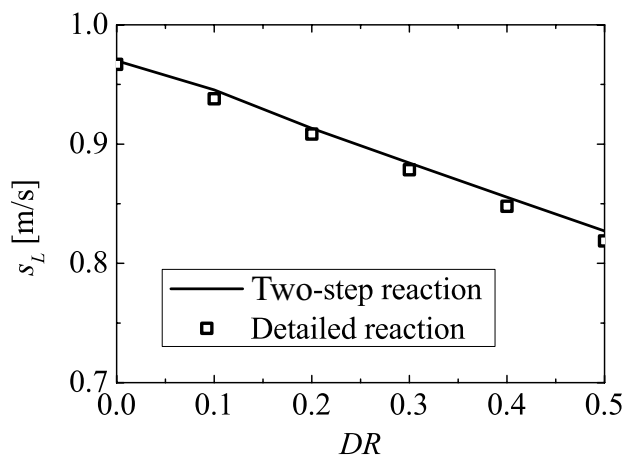
(a)
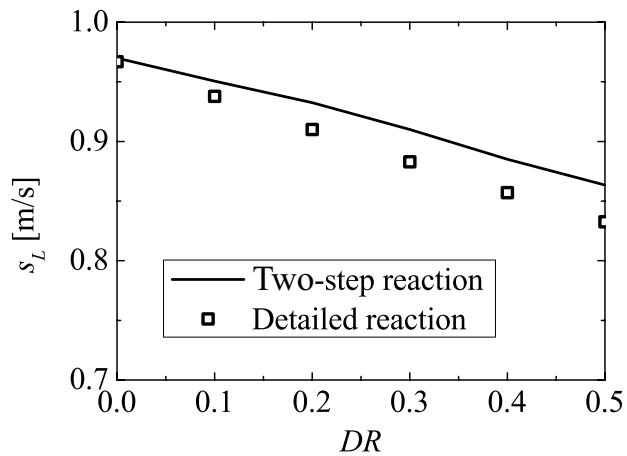
(b)
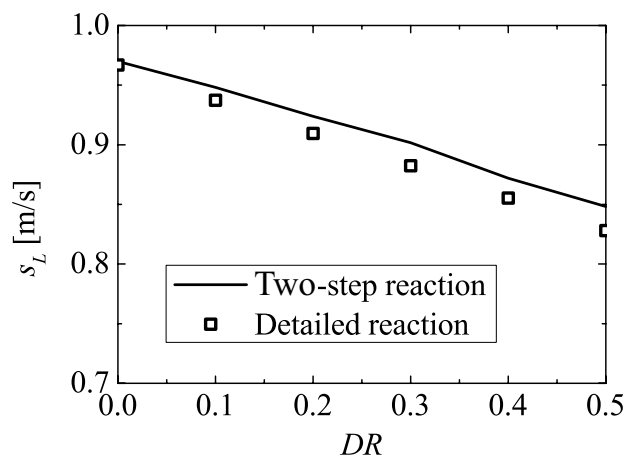
(c)

Figure 8: Comparison of laminar flame speed s_L of volatile matter diluted by (a) H_2O, (b) CO_2, and (c) mixture of H_2O and CO_2 (H_2O:CO_2=1:1) against dilution rate, DR, between proposed two-step reaction and detailed reaction (Newlands coal, ϕ=1.0).
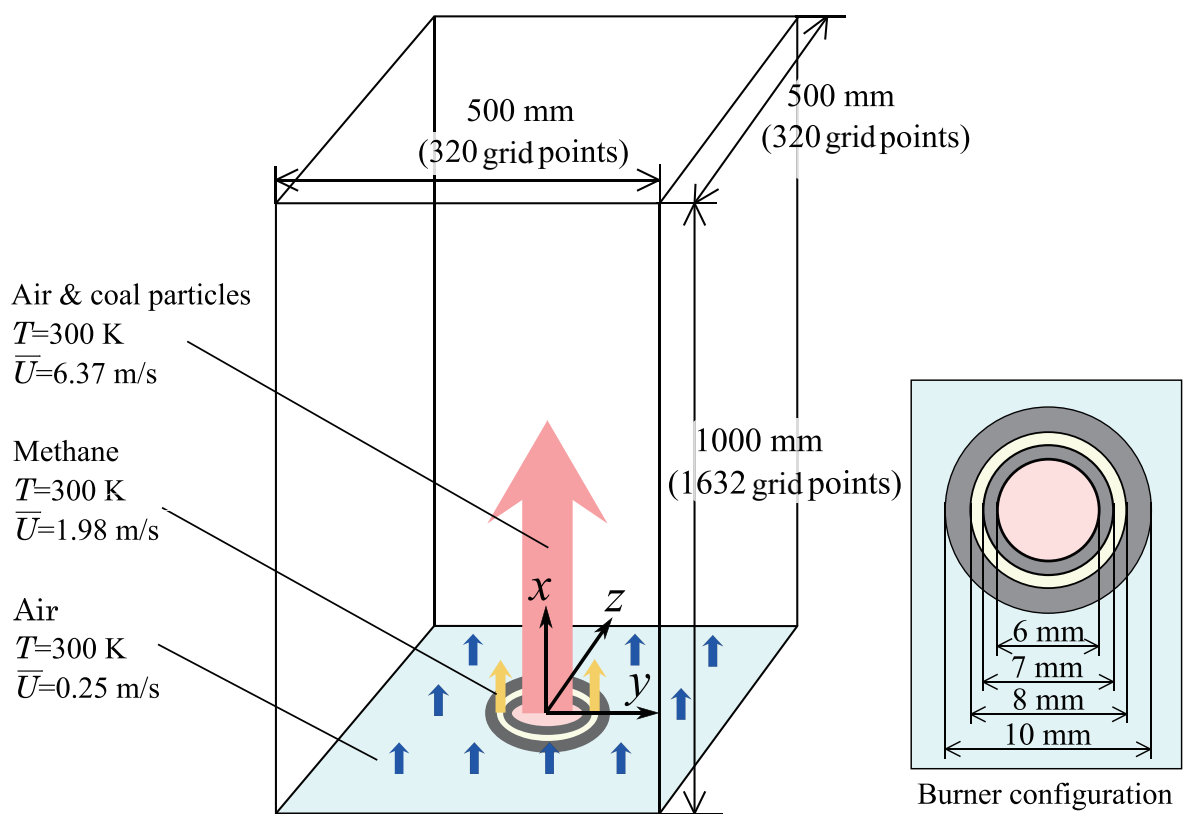
Figure 9: Schematic diagrams of computational domain and inlet boundary conditions.
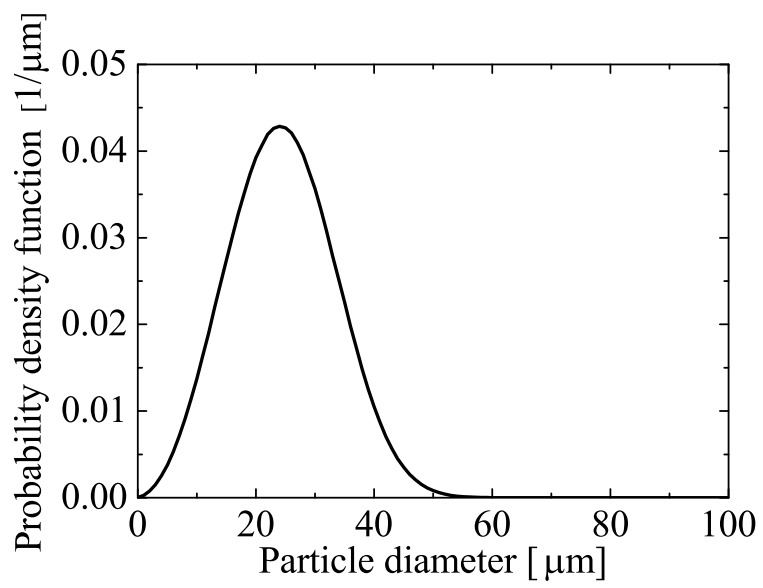
Figure 10: Probability density function of initial coal particle diameter.

0.20 m

0 m

300 ━━━━━ 2200

T [K]

(a)

0 ━━━━━ 0.22

$Y_{C_a H_b O_c}$ [-]

(b)
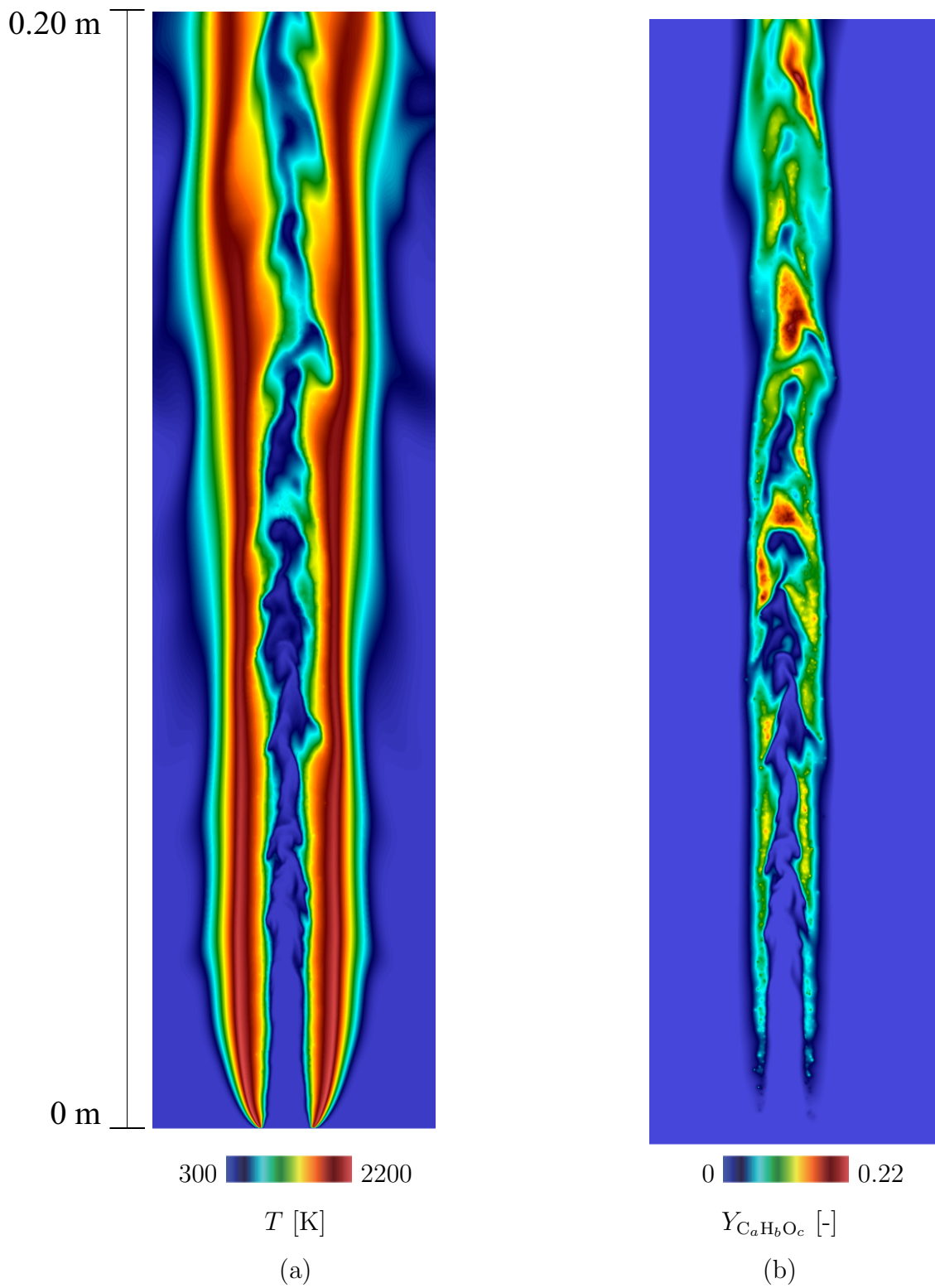
Figure 11: Instantaneous distributions ($x - y$ plane) of (a) gas temperature, T, and (b) mass fraction of volatile matter, $Y_{C_a H_b O_c}$.

47
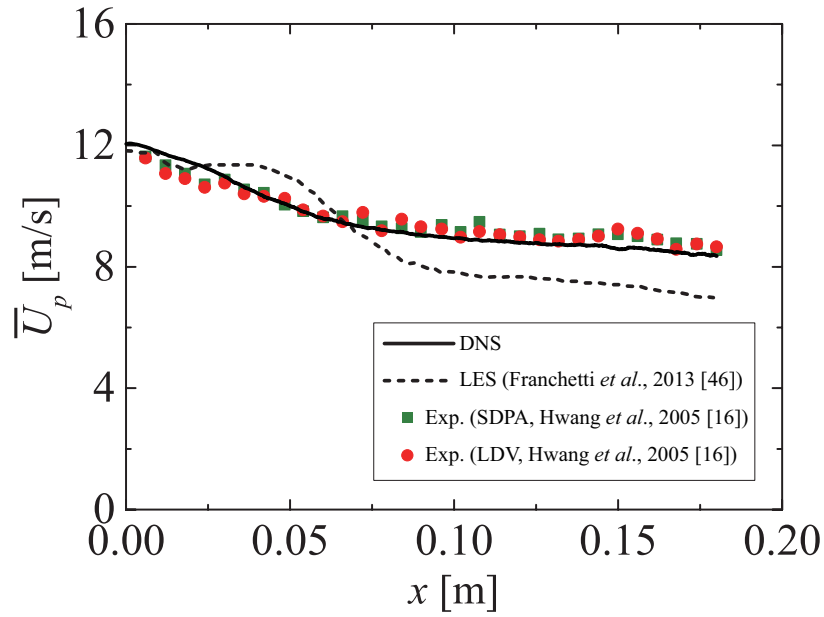
(a)
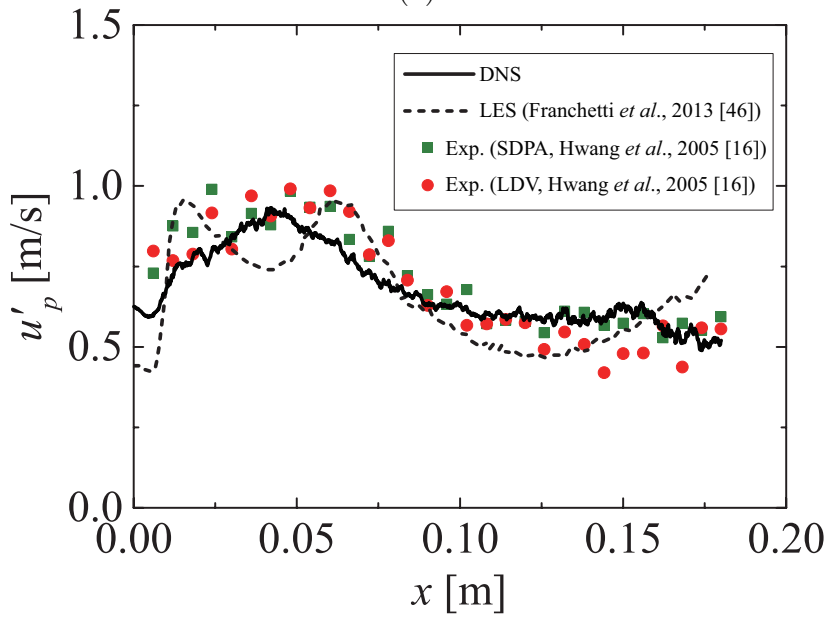
(b)

Figure 12: Comparisons of streamwise profiles of (a) mean streamwise particle velocity, $\overline{U_p}$, and (b) root mean square of streamwise particle velocity fluctuation, $u_p{}'$, on the central axis among DNS, LES [46] and experiment [16].
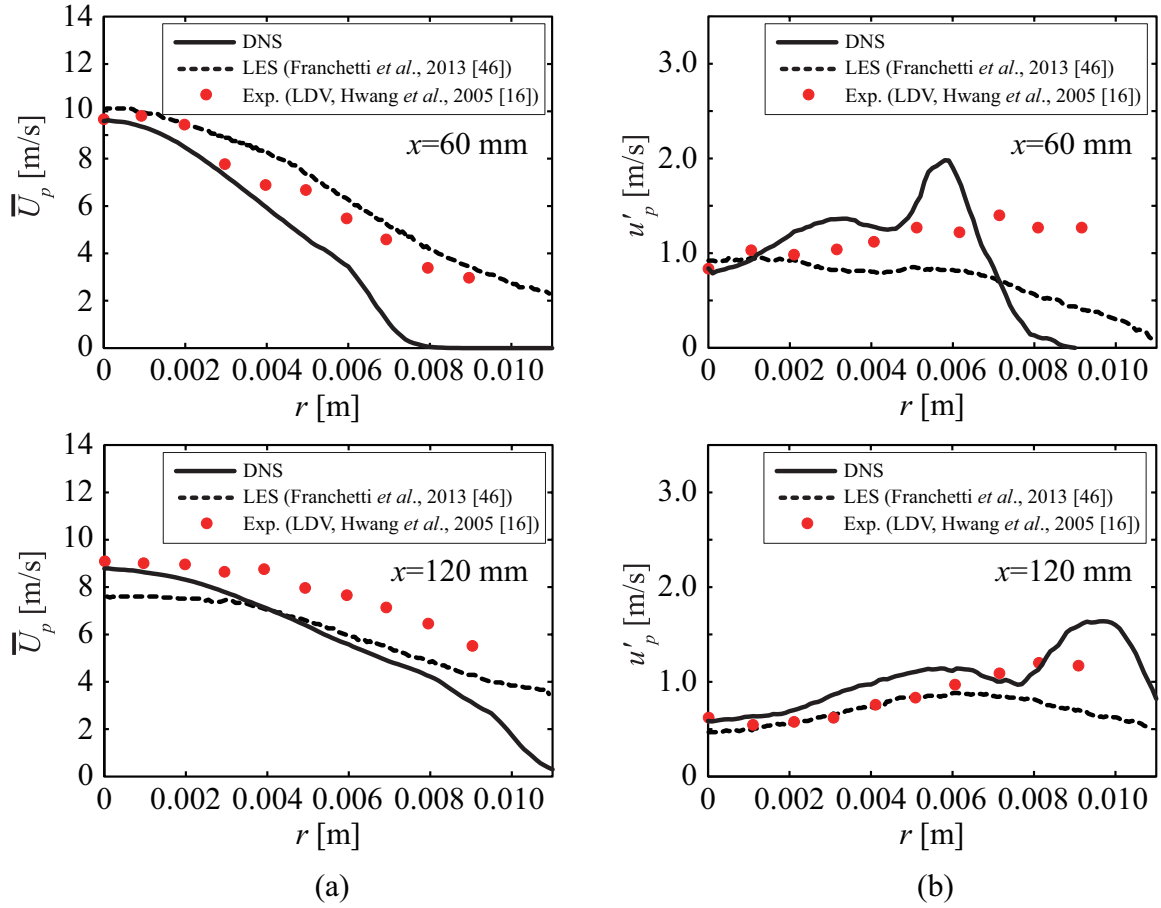
Figure 13: Comparisons of radial profiles of (a) mean streamwise particle velocity, $\overline{U_p}$, and (b) root mean square of streamwise particle velocity fluctuation, u_p', at $x = 60$ mm and 120 mm from the burner inlet among DNS, LES [46] and experiment [16].

0.195 m

0.015 m

(a)   (b)
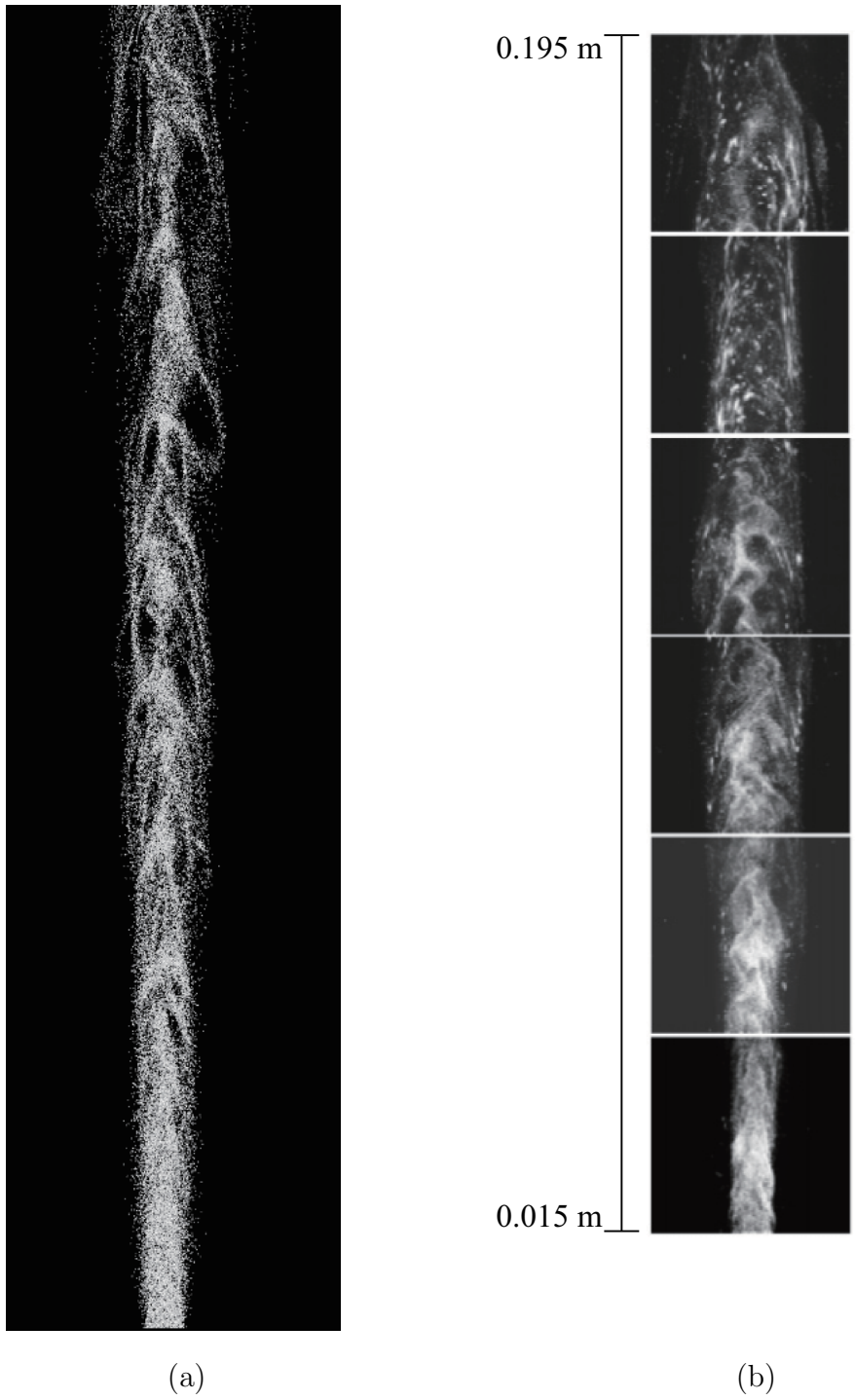
Figure 14: Comparison of instantaneous coal particle distribution ($x - y$ plane) between (a) DNS and (b) experiment [16].
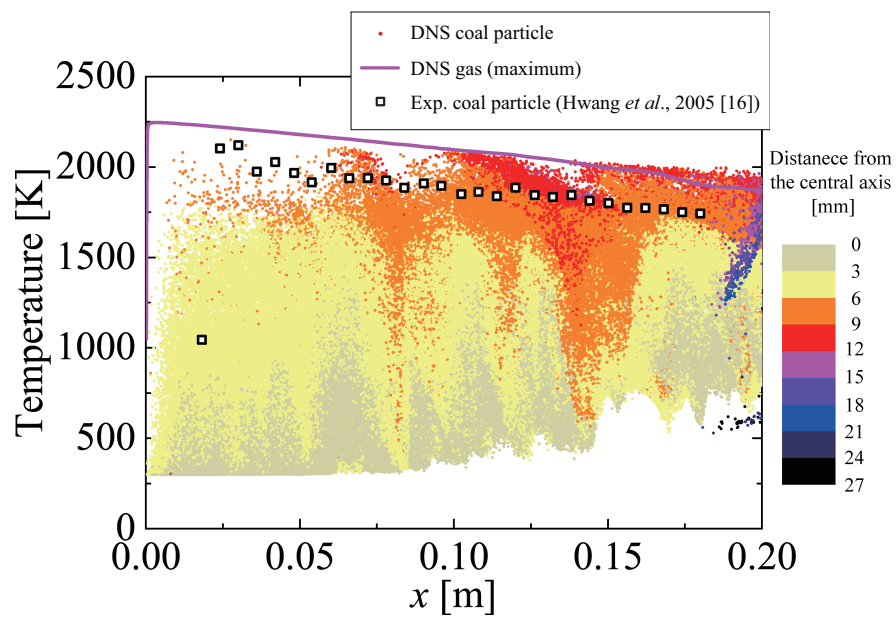
Figure 15: Comparison of coal particle temperatures among DNS and experiment [16], and maximum gas temperature by DNS.
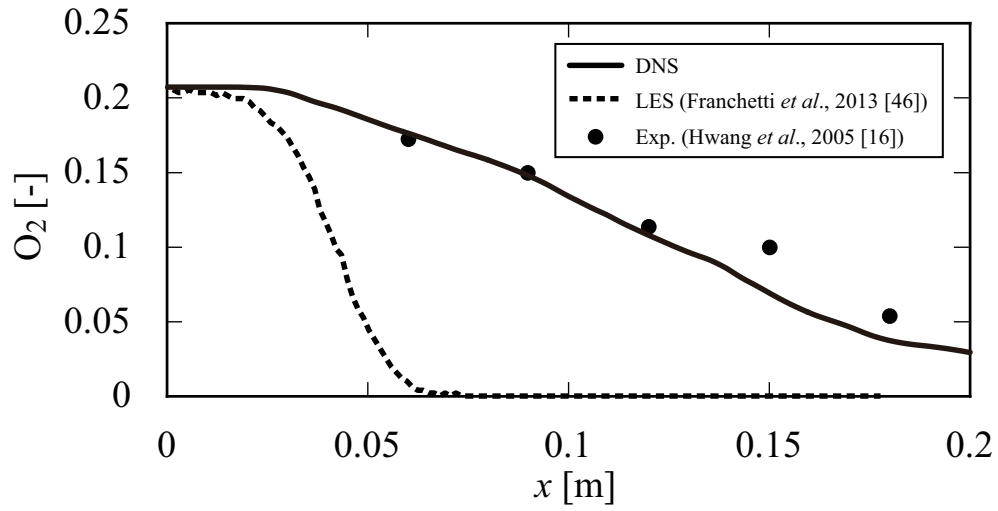
(a)
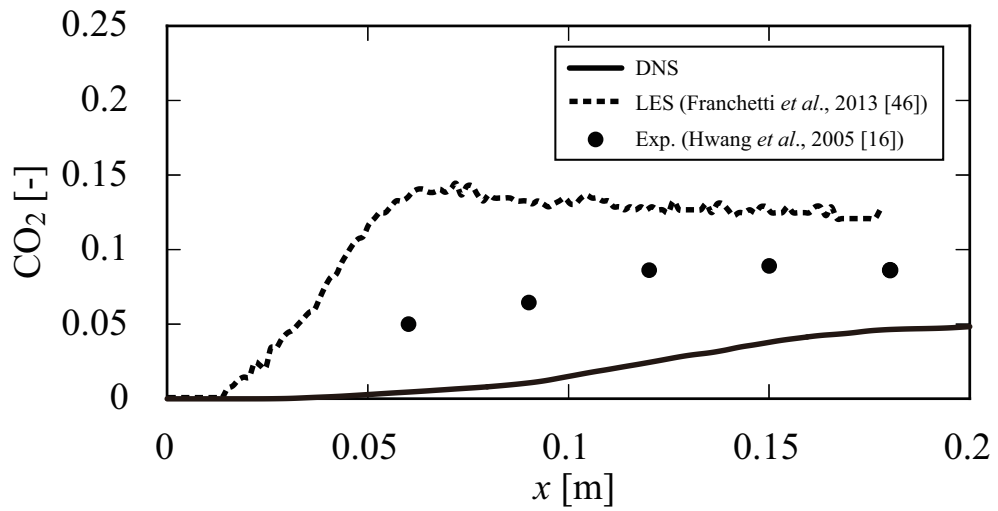
(b)

Figure 16: Comparisons of streamwise profiles of mean chemical species concentrations (mole fractions) of (a) O_2 and (b) CO_2 on the central axis among DNS, LES [46] and experiment [16].
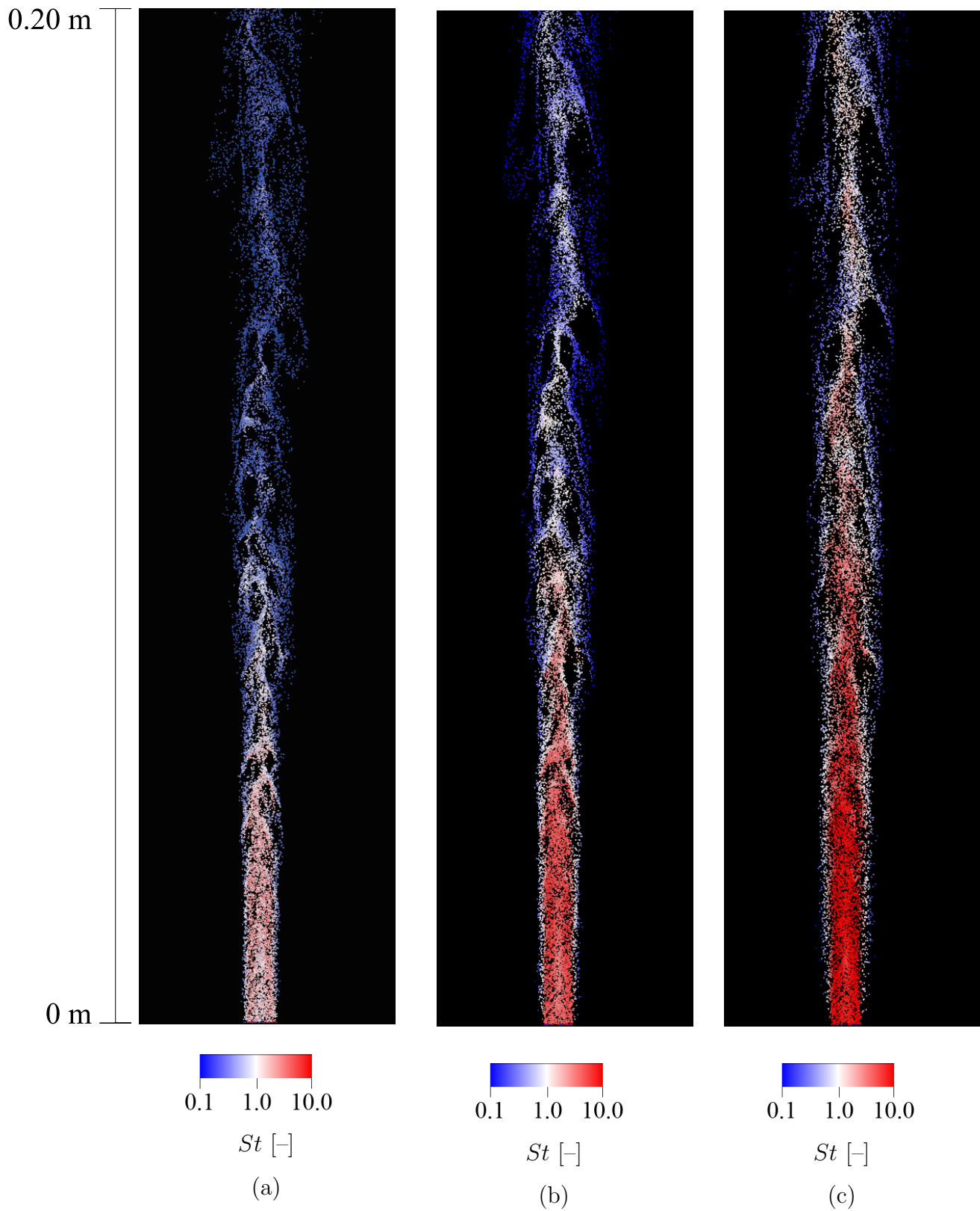
Figure 17: Instantaneous coal particle distributions ($x - y$ plane) and Stokes number, St, of each particle with diameters of (a) 10–18.5 μm, (b) 21.5–26 μm and (c) 31–40 μm.
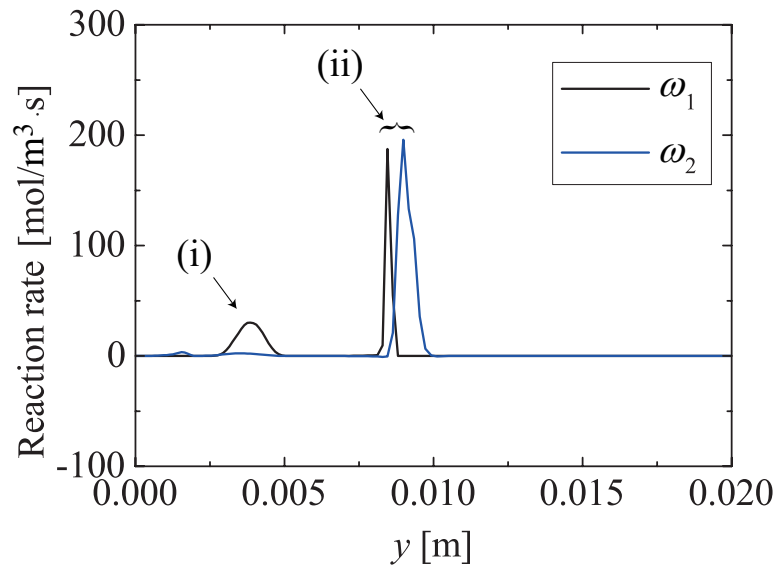
0.20 m

0 m

(diffusion) -500   500 (premixed)

F.I. $[1/\text{m}^2]$
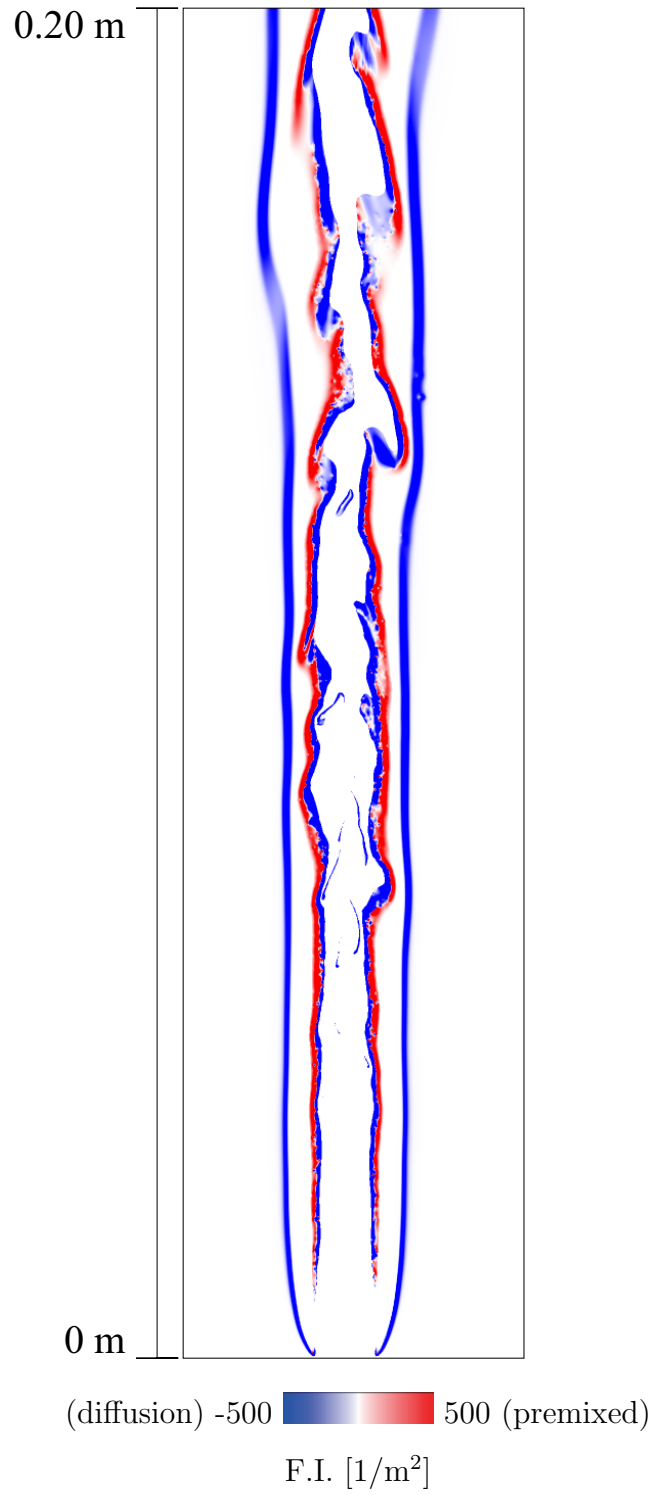
Figure 18: Instantaneous distribution ($x - y$ plane) of flame index, F.I.

54
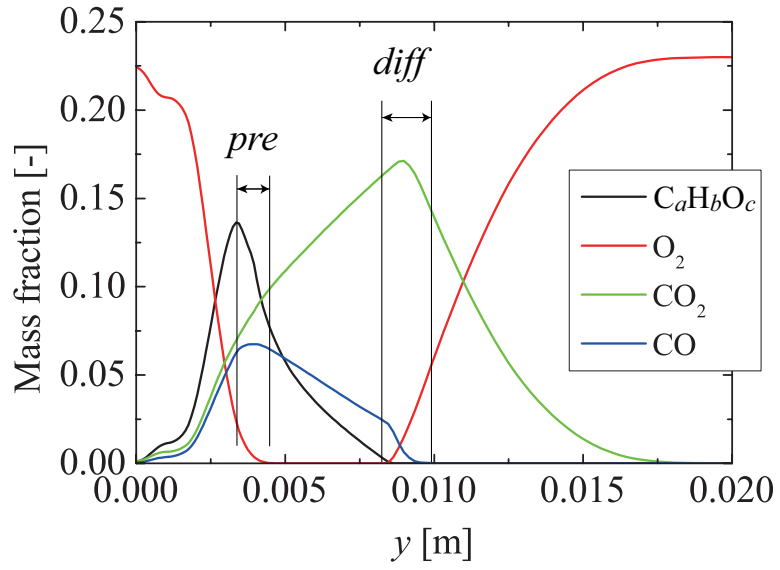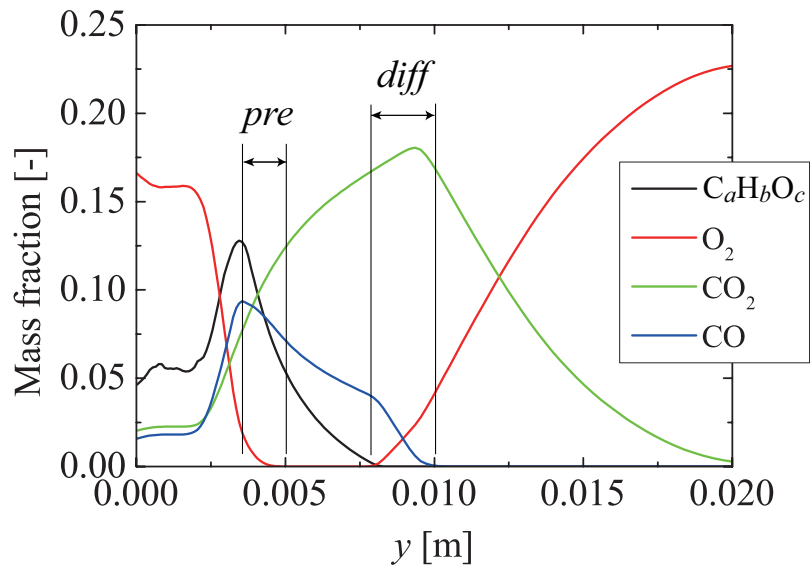
(a)

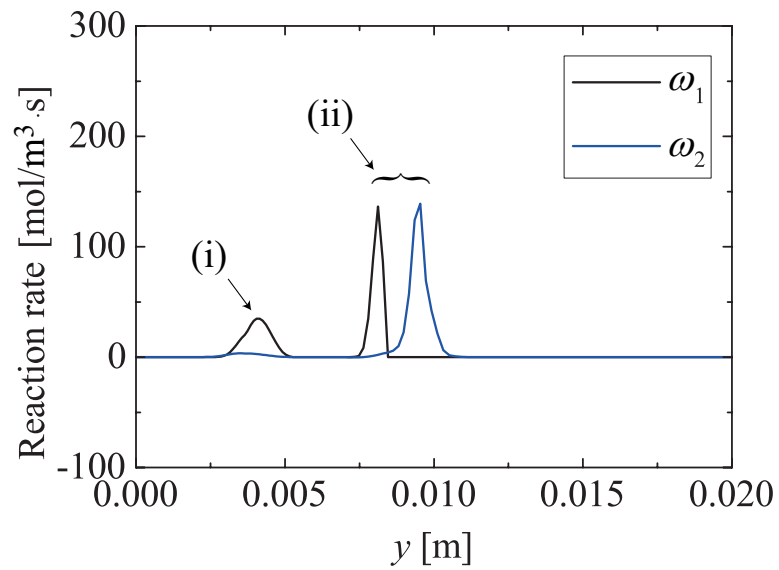(b)

Figure 19: Spanwise profiles of instantaneous (a) mass fractions of $C_aH_bO_c$, O_2, CO_2 and CO and (b) reaction rates of $C_aH_bO_c$ and CO, ω_1 and ω_2, at $x = 60$ mm. (i) and (ii) in the Fig. 19(b) indicate the premixed and the diffusion flame region, respectively.

(a)

(b)

Figure 20: Spanwise profiles of instantaneous (a) mass fractions of $C_aH_bO_c$, O_2, CO_2 and CO and (b) reaction rates of $C_aH_bO_c$ and CO, ω_1 and ω_2, at $x = 120$ mm. (i) and (ii) in the Fig. 20(b) indicate the premixed and the diffusion flame region, respectively.
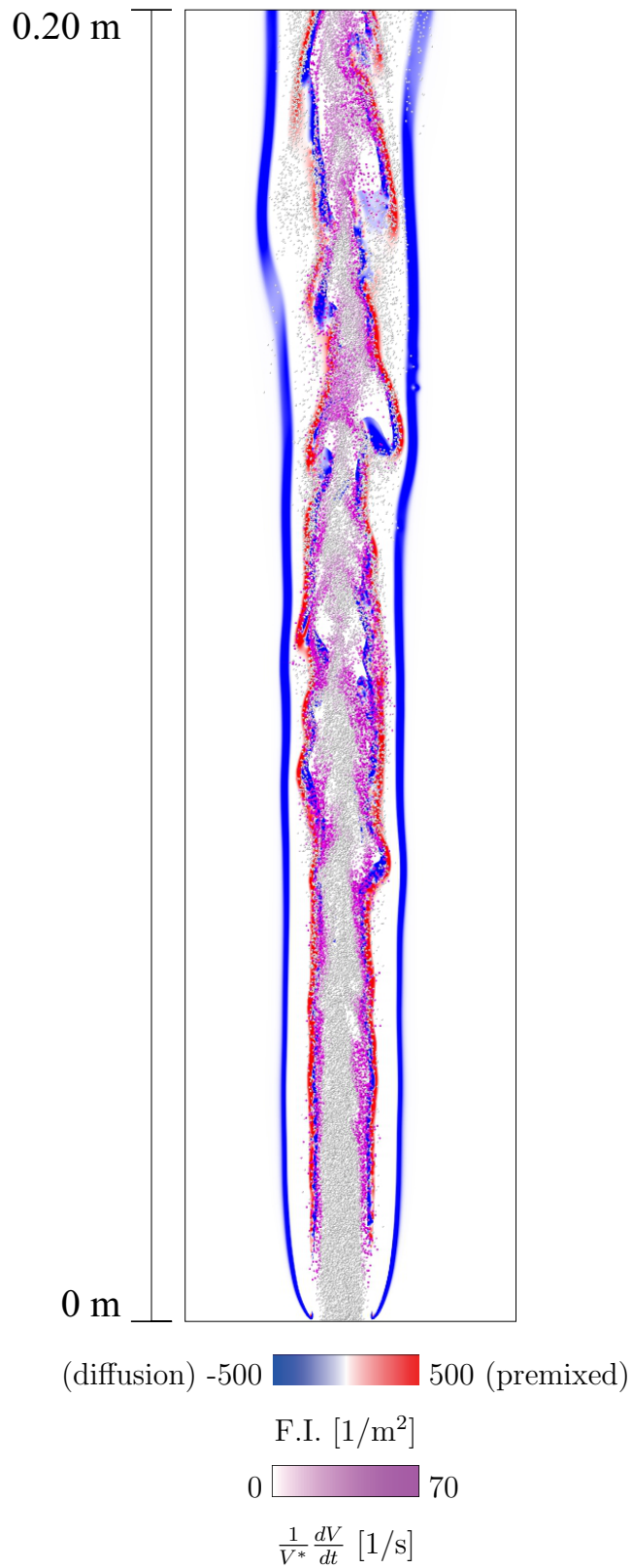
Figure 21: Instantaneous distributions ($x - y$ plane) of normalized devolatilization rate for each particle, $\frac{1}{V^*}\frac{dV}{dt}$, and flame index, F.I.